A tripartite organelle platform links growth factor receptor signaling to mitochondrial metabolism

Deborah Salvi Mesa[1,2*], Elisa Barbieri[2*], Andrea Raimondi[3*], Stefano Freddi[1,2], Giorgia Miloro[2], Gorana Jendrisek[2], Giusi Caldieri[2], Micaela Quarto[1,2], Irene Schiano Lomoriello[1,2], Maria Grazia Malabarba[1,2], Arianna Bresci[4], Francesco Manetti[4], Federico Vernuccio[4], Hind Abdo[5], Giorgio Scita[1,5], Dario Polli[4,6], Carlo Tacchetti[3,7], Paolo Pinton[8], Massimo Bonora[8], Pier Paolo Di Fiore[1,2#], Sara Sigismund[1,2#]

[1]Department of Oncology and Hematology-Oncology, Università degli Studi di Milano, Milan Italy
[2]IEO, European Institute of Oncology IRCCS, Milan, Italy
[3]Experimental Imaging Centre, IRCCS San Raffaele Scientific Institute, Milan, Italy
[4]Department of Physics, Politecnico di Milano, Milan, Italy
[5]IFOM, The AIRC Institute of Molecular Oncology, Milan, Italy
[6]CNR Institute for Photonics and Nanotechnology (CNR-IFN), Milan, Italy
[7]Vita-Salute San Raffaele University, Milan, Italy
[8]Department of Medical Sciences, Section of Experimental Medicine and Laboratory for Technologies of Advanced Therapies (LTTA), University of Ferrara, Ferrara, Italy

* These authors contributed equally; # SS and PPDF jointly supervised this work.

Correspondence: to SS, sara.sigismund@ieo.it or to PPDF, pierpaolo.difiore@ieo.it

Abstract

One open question in the biology of growth factor receptors is how a quantitative input (*i.e.,* ligand concentration) is decoded by the cell to produce specific response(s). Here, we show that an EGFR endocytic mechanism, non-clathrin endocytosis (NCE), which is activated only at high ligand concentrations and targets receptor to degradation, requires a tripartite organelle platform involving the plasma membrane (PM), endoplasmic reticulum (ER) and mitochondria. At these contact sites, EGFR-dependent, ER-generated Ca^{2+} oscillations are sensed by mitochondria, leading to increased metabolism and ATP production. Locally released ATP is required for cortical actin remodeling and EGFR-NCE vesicle fission. The same biochemical circuitry is also needed for an effector function of EGFR, i.e., collective motility. The multiorganelle signaling platform herein described mediates direct communication between EGFR signaling and mitochondrial metabolism, and is predicted to have a broad impact on cell physiology as it is activated by another growth factor receptor, HGFR/MET.

INTRODUCTION

Epidermal growth factor (EGF) receptor (EGFR) signaling controls multiple cellular phenotypes, including proliferation, migration, differentiation, apoptosis and stem cell regulation[1, 2]. This variety of outputs is, in part, achieved through the multiplicity of ligands and/or EGFR heterodimerization with other ErbB family receptors[2]. However, the same ligand can induce multiple cellular responses not only in different cellular contexts, but also in the same cell type as a function of its concentration and duration of exposure[3, 4]. How the cell decodes the quantitative growth factor input into a specific cellular response is not completely understood.

We recently discovered a close crosstalk between EGFR endocytosis and interorganelle communication[5]. Clathrin-mediated endocytosis (CME) is the preferred route at limiting EGF concentrations (≤1 ng/ml), while at higher EGF concentrations (≥10 ng/ml) non-clathrin endocytosis (NCE) is also activated[6, 7]. Since CME sustains signaling and the EGF-induced mitogenic response by recycling receptor back to the plasma membrane (PM) and NCE attenuates signaling by targeting receptor to lysosomal degradation, the relative contribution of each route to EGFR internalization dictates signaling intensity and thus cellular response[8].

EGFR-NCE involves interorganelle communication by way of contact sites between the PM and endoplasmic reticulon (ER) that are dependent on the cortical ER-resident protein Reticulon-3 (RTN3) [5]. While the long isoform of RTN3 is implicated in endosome maturation and autophagy[9, 10], the short isoform is involved in EGFR-NCE[5]. The ER-PM contacts are formed upon EGFR activation and serve as anchors for PM tubular invaginations (TIs) and hot spots of localized calcium signaling triggered by Ca^{2+} released from the ER via the inositol-3-phosphate receptor (IP3R). This Ca^{2+} response is essential for TI fission and subsequent release of NCE vesicles into the cytosol[5]. However, given the pleiotropic roles of Ca^{2+} it is possible that the EGFR-NCE Ca^{2+} response has wider implications in the cell.

Herein, we provide evidence that EGFR-NCE internalizing structures participate in PM-ER-mitochondria contact sites which constitute a multiorganelle signaling platform where Ca^{2+} oscillations are sensed by mitochondria leading to an upregulation of mitochondrial cofactors (NAD(P)H and FAD) and ATP production. We took advantage of different tools to measure mitochondrial activity, both globally (*i.e.,* with dyes detecting mitochondrial membrane potential and label-free two-photon excitation fluorescence (TPEF) detecting endogenous nonlinear fluorescence of mitochondrial cofactors) and in a spatially resolved manner (*i.e.,* exploiting calcium probes and the ATP-dependent enzyme, luciferase, targeted to specific cellular compartments). The increase in mitochondrial energetics in turn regulates cortical actin remodeling which is needed for the completion of EGFR-NCE internalization and for inducing collective cell migration. This work

directly links EGFR signaling to mitochondrial metabolism via the establishment of a physical and functional interaction between organelles, and demonstrates how a quantitative signal detected at the PM can be deconvoluted into specific cellular responses. This mechanism is relevant for different growth factor receptors, namely EGFR and hepatocyte growth factor receptor (HGFR or MET), and in different epithelial cell contexts, and it is thus predicted to have a broad impact on cellular behaviour.

RESULTS

Tripartite ER-PM-mitochondria contact sites are regulated by high dose EGF

CD147 is a specific NCE cargo that co-internalizes with EGFR in the presence of high dose EGF[5]. Immuno-electron microscopy (EM) of HeLa cells revealed that CD147-NCE internalizing structures are in close contact with ER stacks which, in turn, are in contact with mitochondria (**Fig.1A and Fig. S1A**). 3D tomographic reconstruction confirmed the topological nature of these tripartite contacts showing that an ER tubule is always interposed between NCE PM invaginations and neighboring mitochondria (**Fig. 1B and Movies S1, S2**). Quantification of the ER-mitochondrial contacts by EM tomographic reconstruction (**Fig. 1C**) revealed that high dose EGF treatment increases the fraction of mitochondria with extended areas of contact with the ER (**Fig. 1D**). These EGF-induced ER-mitochondrial contacts were located close to the PM (within 1 μm), while contacts further from the PM were unchanged by EGF treatment (**Fig. 1E**).

To determine the impact of different perturbations on these contact sites, we developed an alternative method for quantifying them that could be applied to multiple samples. This method measures the colocalization of ER and mitochondrial markers in deconvolved fluorescence images of thin sections of resin-embedded cells (**Fig. 1F, left and center,** yellow dots). The accuracy of this approach was confirmed by correlative light electron microscopy (CLEM) (**Fig. 1F, right**), which established a good correlation between the number of contacts identified by fluorescence and by EM (**Fig. S1B**). The fluorescence method confirmed the EM tomography data (**Fig. 1E**) indicating that only high dose EGF increases the number of ER-mitochondrial contacts near to the PM (**Fig. 1G**). Furthermore, the knockdown (KD) of the critical EGFR-NCE regulator, RTN3, inhibited the formation of PM proximal ER-mitochondrial contacts, showing that they are dependent on EGFR-NCE (**Fig. 1G and Fig. S1C**). In contrast, the KD of RTN4, a reticulon family member not involved in NCE[5], did not have an inhibitory effect, but instead appeared to slightly increase the contacts near to the PM. This observation is in line with the reported effects of RTN4 KD on general ER morphology[5, 11], which are however unrelated to NCE[5].

Thus, EGF appears to induce the formation/stabilization of ER-mitochondria contact sites near to NCE PM internalizing structures.

High EGF induces PM-restricted Ca^{2+} waves through the buffering activity of mitochondria

We previously showed that high EGF induces Ca^{2+} release from the ER, via the IP3R channel, at NCE PM-ER contact sites using the Ca^{2+} sensor Aequorin[5]. Here, we investigated the contribution of mitochondria to this Ca^{2+} response, using the Ca^{2+} probe, GCaMP6f[12], which at variance with Aequorin permits measurements of Ca^{2+} oscillations at the single cell level. Using HeLa cells stably transfected with GCaMP6f targeted to the PM inner leaflet (PM-GCaMP6f), we showed that high but not low EGF elicited repetitive Ca^{2+} spikes at the PM (**Fig. 2A,B, Fig. S2A and Movie S3**), which were NCE specific, as shown by their dependency on RTN3 and IP3R, but not on RTN4 (**Fig. 2B and Fig. S2B**). Also, the main CME adaptor protein, AP2, showed a minor impact on EGF-induced Ca^{2+} oscillations at the PM (**Fig. S2C,D**).

The EGF-induced Ca^{2+} oscillations resemble those observed upon agonist stimulation[13], whose generation and propagation require mitochondrial Ca^{2+} buffering at the ER interface[14-16]. Indeed, inhibition of the mitochondrial calcium uniporter (MCU) complex by siRNA or the selective inhibitor MCUi11[17], abolished the EGF-induced Ca^{2+} waves at the PM, similarly to RTN3 and IP3R KD (**Fig. 2C,D and Fig. S2E**). Importantly, the inhibition of MCU did not reduce the Ca^{2+} signaling response at the PM induced by another receptor agonist, *i.e.,* histamine, a well-studied signaling pathway leading to Ca^{2+}release from the ER[18], arguing for specificity in the EGF-induced response at the PM (**Fig. S2F**), at least in the systems herein tested.

Finally, using the GCaMP6m sensor targeted to the mitochondrial matrix (Mito-GCaMP6m, **Fig. 2A right**), we demonstrated that high, but not low, EGF induces Ca^{2+} oscillations inside the mitochondria that were dependent on MCU, IP3R and RTN3, but not on RTN4 (**Fig. 2E,F and Movie S4)**. Similar results were obtained using mitochondrial-targeted Aequorin (mito-Aequorin, **Fig. S2G,H**)[19]. Thus, mitochondria play a pivotal role in EGF-dependent Ca^{2+} buffering at PM-ER-mitochondria tripartite contact sites, and are required to achieve a productive Ca^{2+} signaling oscillatory response at the PM induced by EGF.

EGF-dependent Ca^{2+} oscillations induce changes in mitochondrial energetics

EGF-induced Ca^{2+} oscillations inside the mitochondrion are predicted to affect mitochondrial metabolic functions, first and foremost ATP production. Indeed, the accumulation of Ca^{2+} in the mitochondrial matrix stimulates the activity of Ca^{2+}-dependent dehydrogenases of the Krebs cycle, resulting in elevation of the mitochondrial membrane potential ($\Delta\Psi m$) and ATP production[20]. To

investigate the potential crosstalk between EGFR signaling and mitochondria, we measured the effect of EGF stimulation on ΔΨm using the potentiometric dye TMRM[21]; since ΔΨm is required for ATP production, changes in this parameter act as a proxy for variations in ATP production. High, but not low, EGF rapidly increased TMRM fluorescence intensity (**Fig. 3A,B and Movie S5**), indicative of an increase in ΔΨm and mitochondrial ATP production. This response appeared to be dependent on the Ca^{2+} signaling at NCE contact sites since it was inhibited by RTN3, IP3R or MCU KD and by acute treatment with the MCU inhibitor, MCUi11, but was not decreased by RTN4 or AP2 KD (**Fig. 3C and Fig. S3A,B**).

To confirm the impact of EGF on mitochondrial metabolism, we employed an approach based on label-free TPEF that has been recently characterized as a method to monitor subtle metabolic changes[22, 23]. In particular, the TPEF signal scales linearly with the concentration of mitochondrial cofactors, NAD(P)H and FAD, in the irradiated cell volume. Importantly, we observed that high dose EGF induces a broader distribution of the TPEF signal expanding into the peripheral cytoplasmic areas, whereas the signal in non-stimulated cells and RTN3 KD cells concentrates in the perinuclear region (**Fig. 3D, left**). Quantification of the TPEF signal confirmed a significantly higher percentage of cell area featuring fluorescent mitochondrial co-enzymes in high dose EGF stimulated cells compared with RTN KD and unstimulated cells (**Fig. 3D, right**). These results are in line with the idea that high dose EGF induces an increase in the metabolic activity of peripheral mitochondria by triggering EGFR-NCE.

To investigate further how EGF affects intracellular ATP, we used the ATP-dependent enzyme luciferase, which in the presence of its substrate luciferin emits luminescence as a function of ATP levels [24]. When luciferase was expressed in the cytosol, high dose EGF resulted in a reduction in luminescence indicating the consumption of cytosolic ATP, which was not observed at low EGF doses (**Fig. S3C,D**). However, in cells expressing luciferase targeted to the PM inner leaflet, a peak of luminescence at the subplasmalemmal level was observed immediately after stimulation with high, but not low, EGF (**Fig. 3E,F**, **Fig. S3E**), indicative of a local increase in ATP levels. This increase in ATP appears to be dependent on NCE-associated Ca^{2+} signaling, mitochondrial buffering activity and mitochondrial ATP production since it occurred only in the presence of high dose EGF and was inhibited by RTN3 KD and inhibitors of IP3R (xestospongin C, XeC), MCU (MCUi-11), mitochondrial ATP synthase (oligomycin, OMY) and mitochondrial ADP/ATP translocase which mediates ATP export from mitochondria (bongkrekic acid, BKA), but not by RTN4 KD or AP2 KD (**Fig. 3G,H and Fig. S3F,G**). Of note, RTN4 KD caused an increase in subplasmalemmal ATP levels that might be explained by the increase in mitochondria-ER contacts sites observed in this condition (**Fig. 1G**).

The link between mitochondrial metabolism and NCE - but not CME - was corroborated by observations in a HeLa clone (OSLO) which activate only CME and not NCE upon EGF stimulation[5, 7]. HeLa OSLO cells stimulated with high dose EGF did not show PM-localized Ca^{2+} oscillations nor changes in ΔΨm and subplasmalemmal ATP levels (**Fig. S3H-J**).

Together, these data suggest that the active EGFR, through NCE and the generation of Ca^{2+} waves, can signal to mitochondria in proximity of NCE sites to increase their production of ATP which is then locally released near the PM.

The crosstalk between NCE and mitochondria is observed also for the HGFR

To understand whether the NCE mechanism is relevant to other growth factor receptors, we investigated HGFR (MET) which is is highly expressed in epithelial cells including HeLa[25]. HGFR is activated by its only known ligand, HGF, and like EGFR it can be ubiquitinated by the E3 ligase Cbl, endocytosed and targeted to lysosomal degradation[26, 27]. We therefore stimulated HeLa cells with saturating doses of HGF and followed CD147 internalization (*in vivo*) and HGFR localization (staining it with specific antibody after cell fixation). In unstimulated cells, the HGFR signal was mainly localized at the PM, while only a small amount of CD147 signal was detectable in intracellular vesicles (*i.e.,* after acid wash treatment, **Fig. 4A**). Upon HGF stimulation, HGFR internalization was induced as expected. HGF stimulation also induced the internalization of CD147, which colocalized with intracellular HGFR (**Fig. 4A**). Immuno-EM revealed that, HGF-induced CD147-NCE internalizing structures form tripartite contacts sites with ER cortical tubules and mitochondria (**Fig. 4B**). Importantly, HGFR endocytosis was inhibited by both RTN3 KD and clathrin KD alone, and further decreased upon the double KD, as quantified by an increase in the ratio of PM to total HGFR (**Fig. 4C**). These results suggest that HGFR, similarly to EGFR, can be internalized by both CME and NCE mechanisms. Notably, CD147 internalization was monitored and shown to be independent of clathrin, but requiring RTN3, as expected for this NCE specific marker (**Fig. 4D**). Together, these data show that high dose HGF stimulates the internalization of HGFR through the NCE mechanism in HeLa cells.

Importantly, HGF stimulation induces Ca^{2+} oscillations at the PM, similarly to EGF stimulation, and these oscillations are dependent on NCE (RTN3), the IP3R calcium channel on the ER and mitochondrial buffering activity (MCU) (**Fig. 4E**). Moreover, these PM-localized Ca^{2+} oscillations induced by HGF led to rapid changes in mitochondrial energetics dependent on the same molecular circuitry (**Fig. 4F**). These results extend the relevance of NCE beyond the EGFR system, showing that HGFR activates the same circuitry influencing calcium signalling and mitochondrial energetics similarly to EGFR.

Mitochondrial Ca^{2+} buffering activity and localized mitochondrial ATP production are required for NCE vesicle fission

To investigate the role of the crosstalk between EGFR and mitochondria in NCE, we inhibited the different steps of this signaling and assessed effects on the internalization of the NCE cargo CD147[5]. Inhibition of Ca^{2+} release (IP3R KD) or mitochondrial buffering activity (MCU KD or MCUi11 inhibitor treatment) inhibited CD147-NCE (**Fig. 5A and Fig. S4A**), without affecting the internalization of the CME cargo transferrin (Tf) (**Fig. S4B**). Next, we acutely inhibited mitochondrial ATP production by short treatment (5 min) with the mitochondrial ATP synthase inhibitor OMY. This treatment inhibited CD147-NCE (**Fig. 5B top**) as well as EGFR-NCE, but not EGFR-CME. Indeed, OMY inhibited Alexa647-EGF internalization in clathrin KD cells (CME inhibited, NCE active), but not in RTN3 KD cells (CME active, NCE inhibited), showing that it is inhibiting EGFR-NCE and not EGFR-CME (**Fig. 5B bottom, Fig. S4C,D**). In addition, acute OMY treatment did not alter the activation of the EGFR kinase nor its downstream signaling (**Fig. S4E**), and did not induce changes in total cellular ATP levels (**Fig. S4F),** showing that acute treatment with OMY is not altering the overall cytosolic pool of ATP.

Since we showed that high dose EGF induces a localized increase in ATP at the PM, we investigated the effect of selectively depleting this ATP pool. To this end, we used SNAP25-luciferase, not as an ATP sensor, but as an ATP-consuming enzyme. In presence of an excess of luciferin, CD147 internalization was selectively inhibited in cells expressing SNAP25-luciferase, but not in control cells (**Fig. 5C**). In contrast, Tf endocytosis remained unaffected (**Fig. S4G,H**), arguing that NCE selectively requires the PM-localized ATP pool for its execution, at variance with CME.

To understand the role of Ca^{2+} waves and PM-localized ATP in NCE, we studied the formation of NCE TIs upon inhibition of the ER-mitochondrial Ca^{2+}-ATP axis. The inhibition of IP3-mediated Ca^{2+} release from the ER (XeC), of mitochondrial Ca^{2+} uptake (MCU KD), and of mitochondrial ATP production (short-term OMY) resulted in the elongation of NCE TIs to a similar extent as dynamin KD (the GTPase involved in NCE fission, **Fig. 5D and Fig. S4I**)[5]. In contrast, clathrin-coated pits (CCPs) were elongated only upon dynamin KD, which is known to participate in CCP fission during CME (**Fig. 5E**)[28]. These results argue for a role of Ca^{2+} and ATP specifically in the fission of NCE TIs, while dynamin is involved in both CME and NCE.

To understand if Ca^{2+} and ATP are both required in the fission step, or if Ca^{2+} is needed solely to stimulate mitochondrial ATP production, we performed a CD147 rescue experiment in MCU KD cells where both Ca^{2+} waves and ATP production are inhibited. In these cells, we induced a Ca^{2+} burst independent of the EGF-NCE circuitry by stimulation with histamine (**Fig. S2E**) and/or induced

mitochondrial ATP production independently of Ca^{2+} by feeding the Krebs Cycle with succinate (**Fig. S4L**). We found that only the combination of histamine and succinate was able to rescue CD147 internalization in MCU KD cells (**Fig. 5F**), indicating that Ca^{2+} signaling and mitochondrial ATP act in concert in the execution of EGFR-NCE.

Ca^{2+} signaling and increased mitochondrial ATP production are required for cortical actin remodeling at NCE sites

Actin polymerization relies on protein machinery that is dependent on Ca^{2+} and ATP[29-31]. While CME requires actin polymerization only when PM tension is elevated[32], different clathrin-independent endocytosis (CIE) mechanisms depend on actin cytoskeleton dynamics for PM deformation and/or for fission[33]. We, therefore, investigated whether the requirement for the Ca^{2+}/ATP axis in EGFR-NCE is to sustain cortical actin remodeling. Inhibition of the key regulators of actin polymerization, Arp2/3 (by the CK666 inhibitor) and N-WASP (by KD), impaired CD147/EGF internalization in HeLa cells stimulated with high EGF but did not affect Tf-CME (**Fig. 6A and Fig. S5A,B**). Moreover, Arp2/3 inhibition impaired NCE TI fission (as measured by the ratio between long and short TIs), while it had no effect on CCP fission (**Fig. 6B,C**). Inhibition of actin polymerization was synergistic with dynamin KD in increasing the length of NCE TIs but not of CCPs (**Fig. 6B,C**), indicating that actin and dynamin cooperate in NCE TI fission.

EGF stimulation is known to increase F-actin remodeling inducing extensive cellular ruffling (**Fig. S6C**, left and middle panels)[34]. Mechanistically, high EGF induces Arp2/3 relocalization to the PM, at variance with low EGF (**Fig. S5C**, right panel). Using a cortical actin polymerization probe called MPAct[35], we found that high, but not low dose of EGF induced extensive cortical actin polymerization which peaks after 5 min of EGF stimulation (**Fig. 6D,E and Fig. S5D,E**). This polymerization was dependent on NCE and the Ca^{2+}/ATP axis, as witnessed by its abrogation upon KD and/or inhibition of RTN3, IP3R, MCU or mitochondrial ATP synthase, while RTN4 KD and AP2 KD had no effect (**Fig. 6F,G and Fig. S5F**). These data support a model where NCE requires the interplay between the PM, ER and mitochondria to generate Ca^{2+} waves and localized mitochondrial ATP production, which are in turn needed for cortical actin remodeling that cooperates with dynamin in the fission of NCE TIs.

EGFR signaling and mitochondrial activity at tripartite contact sites are required for EGF-induced cell migration

We asked whether the EGF-induced multiorganelle platform has implications for EGFR signaling and biological output, focusing on collective migration which depends on functional NCE[36]. Given

the relevance of EGFR-NCE in keratinocytes, we used human HaCaT cells, since they are extensively used as a model for cell migration and wound healing induced by growth factors[37].

First, we confirmed that the EGFR-NCE mechanism is conserved in HaCaT cells, as demonstrated by the RTN3/IP3R/MCU-dependent internalization of CD147 and EGF after stimulation with high dose EGF (**Fig. 7A** and **Fig. S6A-C**). Tf internalization was also used as a negative control (**Fig. S6D**). We also verified the generation of RTN3-dependent PM localized Ca^{2+} waves (**Fig. 7B,C and Fig. S6E**) and an increase in $\Delta\Psi m$ at high dose EGF in these cells (**Fig. 7D and Fig. S6F**).

In a wound healing assay, high EGF treatment significantly increased cell migration velocity compared to low EGF which behaved like the serum starved control (**Fig. 7E and Movie S6**). This increased migration velocity was dependent on RTN3, ER-mediated Ca^{2+} release, mitochondrial buffering activity, mitochondrial ATP production and actin polymerization, as demonstrated by RTN3 KD or inhibitor treatments (**Fig. 7F**). Thus, the NCE tripartite organelle platform controls novel aspects of the EGFR signaling response that impinge on mitochondrial ATP metabolism and collective cell migration.

DISCUSSION

Interorganelle contact sites are critical to many cellular physiological processes since, by controlling the transfer of ions, proteins and lipids between organelles, they regulate organelle dynamics and intracellular signaling[38-41]. Herein, we show that tripartite contact sites involving the PM, the ER and mitochondria, are transiently formed upon stimulation of cells with high doses of EGF. These structures are involved in at least two EGF-dependent functions (**Fig. 7G**): i) they execute the process of EGFR-NCE which leads to receptor degradation and signaling attenuation[5]; ii) they act as signaling platforms to induce collective cell migration. This latter finding is relevant to the pleiotropic cellular phenotypes induced by EGF, which acts as a potent mitogen when used at low concentrations[42-44], whereas at higher doses, it elicits a collective migratory response [REF[36, 45] and this paper]. Our findings shed light on how a quantitative signal (i.e., ligand concentration) is deconvoluted into specific cellular responses through the dose-dependent formation of a multiorganelle signaling platform.

Mechanistically, a complex cascade of events takes place at the multiorganelle platform. First, EGF (at high doses only) triggers the formation of ER-mitochondrial contacts in proximity of the PM. We have shown previously that high doses of EGF induce the formation of PM-ER contacts with subsequent release of Ca^{2+} from the ER through IP3R, close to the PM[5]. Since it has been demonstrated that these Ca^{2+} waves can stimulate the association of the ER with mitochondria[46, 47], it

is very likely that the formation of the tripartite complex is directly induced by EGF through this mechanism. Second, we show that the recruited mitochondria perform a dual function. On the one hand, they permit the creation of Ca^{2+} oscillations, in keeping with their known Ca^{2+} buffering activity [14-16]. This ensures that intermittently high Ca^{2+} concentrations are maintained in the vicinity of the platform, preventing the feedback closure of the IP3R channel by Ca^{2+} [48]. On the other hand, the consequent Ca^{2+} oscillations inside the mitochondria are sensed by the mitochondrial Krebs cycle enzymes and ATP synthase machinery, increasing NAD(P)H/FAD and ATP production[20]. Ca^{2+} and ATP released in the microenvironment of the platform are in turn needed to complete EGFR-NCE, via the induction of cortical actin cytoskeleton remodeling, which, together with dynamin, is required for the fission step of NCE-TIs (see proposed model in **Fig. 7G**). The same chain of events is required for collective cell migration, arguing that the cortical actin rearrangements occurring at the multiorganelle platform is also key to this phenotype.

There is vast availability of ATP in the cell (in mM concentrations), so why is a burst of ATP at the PM needed for cortical actin remodeling and vesicle fission? One explanation could be the higher energy requirement and the increased consumption of ATP required for the execution of the EGFR-NCE program compared to other endocytic programs, e.g., EGFR-CME. Indeed, in the first phase of EGFR-NCE, the formation of ER-PM contacts is needed to allow PM invagination and TI elongation, two energy-demanding processes[49, 50]. In agreement, we observed a decrease in cytosolic ATP upon high dose EGF stimulation (**Fig. S3C,D**). In a second phase of EGFR-NCE, mitochondria are strategically positioned in proximity to ER-PM contact sites and provide an extra burst of ATP necessary to induce Arp2/3 relocalization at the PM and cortical actin polymerization, required to complete the fission event, in concert with dynamin. In contrast, CME differs in its energy demands. In the first step of membrane bending and vesicle formation, the clathrin triskelion self-assembles into a polyhedral coat surrounding the membrane in a self-sustaining process that does not require ATP [49, 51]. This leaves the cytosolic pool of ATP available for the fission of CCPs operated by dynamin.

Similar considerations may apply to the migratory phenotype. Mitochondria are involved in the control of cell migration through their role in Ca^{2+} signaling and energy production[52-54]. Moreover, there is evidence that mitochondrial movement can match energy demands throughout the cell[55, 56] and that repositioning of mitochondria at cell periphery is needed for cancer cell migration and invasion[57-60].

One final question is why an effector (migration) and an attenuation (internalization/degradation) mechanism are integrated at the tripartite structures. When we originally discovered that EGFR-NCE is primarily coupled to receptor degradation, as opposed to CME that is coupled to receptor recycling

and signaling sustainment, we proposed that its major function could be to protect the cell from overstimulation[5, 8]. Our present findings highlight a more complex picture where the same signaling platform enacts a specific concentration-dependent effector phenotype while ensuring its termination when no longer needed.

Importantly, we show here that another growth factor receptor, HGFR/MET, exploits the same NCE mechanism and activates the same circuitry influencing calcium and mitochondrial energetics as the EGFR. Given the vast roles that EGFR and HGFR signaling plays in the physiology of epithelial cells (*e.g.,* ranging from the regulation of proliferation and migration to controlling stem cell homeostasis) and the frequent aberrant regulation of these signalling pathways in human cancers, the discovery of a new mechanism that links their signaling to mitochondrial energetics could provide new insights into novel therapeutic approaches combining EGFR/HGFR- and mitochondria-targeted therapies.

Acknowledgments:

We thank P. De Camilli for HRP-KDEL cDNA, P. Tobias Meyer for cDNA of MPAct-mCherry, CFP-CaaX and YFP-CaaX. We thank Rosalind Gunby for critically editing the manuscript. We thank the ALEMBIC facility at San Raffaele Scientific Institute, Milan, Italy for support in EM and CLEM analysis, in particular Eugenia Cammarota and Valeria Berno. We thank IEO Technological Units, in particular, Imaging and Flow Cytometry Units, Biochemistry and Structural Biology Unit and Cell Culture Unit.

Funding:

European Research Council ERC-CoG2020 101002280 (SS)

ERC-Synergy 101071470-SHAPINCELLFATE (GS)

Associazione Italiana per la Ricerca sul Cancro grant AIRC IG 24415 (SS)

Associazione Italiana per la Ricerca sul Cancro grant AIRC IG 18621 (GS)

Associazione Italiana per la Ricerca sul Cancro grant 5XMille 22759 (GS)

Associazione Italiana per la Ricerca sul Cancro grant AIRC IG 18988 (PPDF)

Associazione Italiana per la Ricerca sul Cancro grant AIRC IG 23060 (PPDF)

Associazione Italiana per la Ricerca sul Cancro grant MCO 10000 (PPDF)

Associazione Italiana per la Ricerca sul Cancro grant AIRC IG-23670 (PP)

Worldwide Cancer Research grant 20-0094 (SS)

The Italian Ministry of University and Scientific Research grant PRIN 2017 Prot. 2017E5L5P3 (SS, CT, PP)

The Italian Ministry of University and Scientific Research grant PRIN 2020 Prot. 2020R2BP2E (PPDF)

The Italian Ministry of University and Scientific Research grant PRIN 2020 Prot. 2020RRJP5L_005 (CT)

The University of Milan grant PSR2019 (SS)

The Italian Ministry of Health grant RF-2016-02361540 (PPDF).

A-ROSE funding (PP)

Local funds from the University of Ferrara (PP, MB)

Associazione Italiana per la Ricerca sul Cancro AIRC fellowship (EB, GJ and GM)

European Union project CRIMSON under Grant Agreement No. 101016923 (DP)

Author contributions:

Conceptualization: SS, PPDF, MB, PP, GS, CT

Methodology: SS, PPDF, MB, PP, AR, CT, MGM, GS, HA, DP

Investigation: DSM, EB, AR, SF, GM, GJ, GC, ISL, HA, AB, FM, FV

Visualization: DSM, SS, AR, SF, MGM, AB

Funding acquisition: SS, PPDF, PP, CT, DP

Supervision: SS, PPDF

Writing – original draft: SS, PPDF

Writing – review & editing: SS, PPDF, DSM, MB, GS, PP, MGM

Competing interests

The authors declare no competing interests.

Figures and Legends.

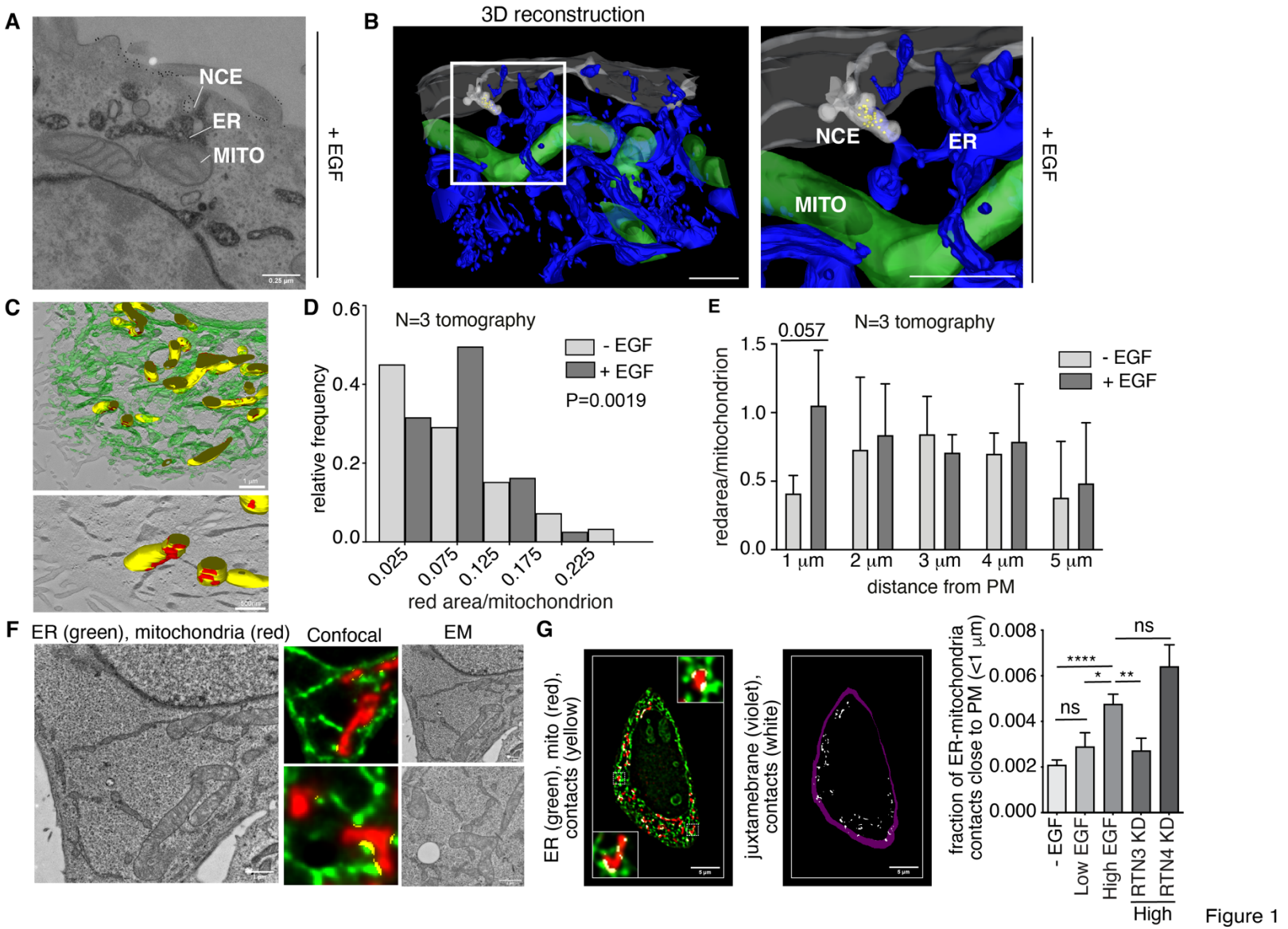

Figure 1

Fig. 1. EGFR-NCE involves tripartite PM-ER-mitochondria contact sites. (A) Representative immuno-electron microscopy image of a CD147-positive NCE structure in contact with the ER, which is, in turn, in contact with a mitochondrion. HeLa cells were stimulated with high dose EGF for 5 min at 37°C. CD147 was immunolabelled with gold. The ER was stained with HRP-KDEL. Bar, 0.25 µM. (**B**) Tomographic 3D reconstruction of the cortical region of a HeLa cell treated and analyzed as in "A" showing the spatial proximity between internalizing NCE structures (light grey) containing the cargo CD147 (yellow dots), the ER (blue) and mitochondria (MITO, green). The ER was automatically recognized through HRP-KDEL staining, while mitochondria were manually segmented. Right, magnification. Bar, 1 µm. (**C**) Upper panel, tomographic 3D reconstruction of the ER (green) and mitochondrial networks (yellow) in HeLa cells treated as in (A). The ER and mitochondria were recognized as in (B). Lower panel, the ER signal was removed and areas of contact (<20 nm) between the ER and mitochondria are highlighted in red. Bars, 1 µM (upper) and 500 nm (lower). (**D**) Quantification of the red area/mitochondrion as in "C" in unstimulated cells *vs.* high dose EGF stimulated cells. Results are expressed as a histogram showing the frequency of mitochondria displaying an *ad hoc* defined range of red area/mitochondrion ratios relative to the total of mitochondria. Pvalue **, <0.01 computed as Chi's square test of the absolute values (N, number of tomograms=3). (**E**) The fraction of mitochondria in contact with the ER (<20 nm) was determined as in (C) and is reported as a function of distance from the PM. Mean ± SD is reported. (**F**) Left, representative deconvolved image of a thin section of resin embedded HRP-KDEL transfected HeLa cells. Center/right, cells were stained with FITC-Tyramide (ER in green) and mitotracker (mitochondria in red). Representative CLEM images used for validation of the assay showing fluorescence (center) and EM (right) images of the same ultrathin sections of cell (see also Figure S1B). Contact sites were recognized by the ImageJ JACoP plugin and are indicated in yellow. Bars, 1 µm. (**G**) Control, RTN3 KD and RTN4 KD HeLa cells were transfected with HRP-KDEL and stimulated with high or low dose EGF or left untreated. Left, representative deconvolved image of resin thin section of HRP-KDEL transfected HeLa control cells stained with FITC-Tyramide (ER in green) and TOMM20 (mitochondria in red) used for ER-mitochondria contact quantification. Center, ER-mitochondria contacts are highlighted in white, while the juxtamembrane region corresponding to the analysis shown on the right is highlighted in violet. Right, ER-mitochondria contacts were quantified with the ImageJ JACoP plugin and their density in the juxtamembrane area was calculated. Bar, 5 µm. Mean density of ER-mitochondrial contacts within 1 µm from the PM ± SEM is reported. N=number of cells: -EGF N=44, Low EGF N=28, High EGF N=78, RTN3 KD N=50, RTN4 KD N=34; p-values in this and other figures were calculated with Each Pair Student's t-test, two-tailed: ****, <0.0001; ***, <0.001; **, <0.01; *, <0.05; ns, not significant.

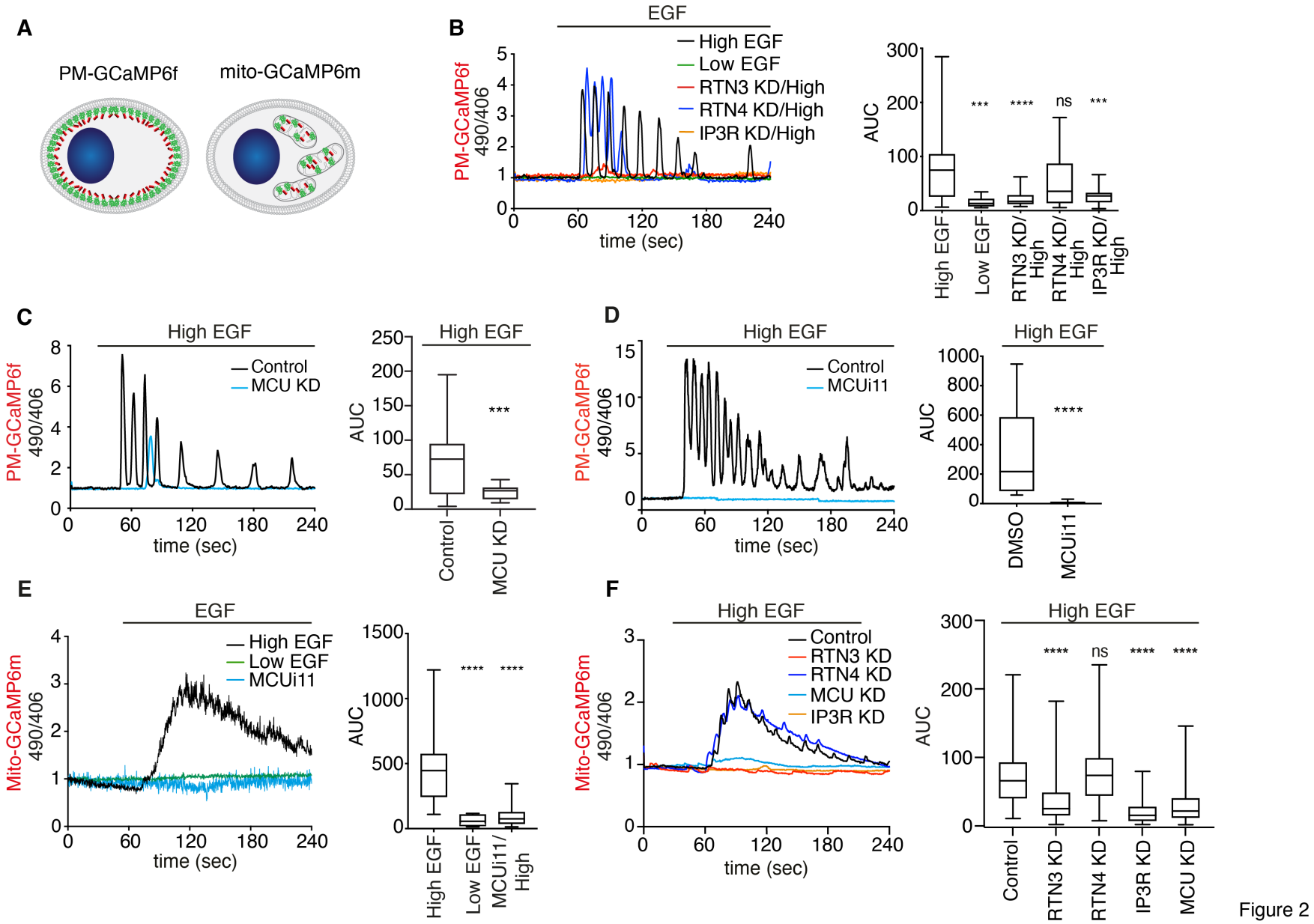
A
PM-GCaMP6f
mito-GCaMP6m
B
EGF
High EGF
Low EGF
RTN3 KD/High
RTN4 KD/High
IP3R KD/High
PM-GCaMP6f 490/406
time (sec)
AUC
***
****
ns
***
High EGF
Low EGF
RTN3 KD/ High
RTN4 KD/ High
IP3R KD/ High
C
High EGF
Control
MCU KD
PM-GCaMP6f 490/406
time (sec)
AUC
***
Control
MCU KD
D
High EGF
Control
MCUi11
PM-GCaMP6f 490/406
time (sec)
AUC
****
DMSO
MCUi11
E
EGF
High EGF
Low EGF
MCUi11
Mito-GCaMP6m 490/406
time (sec)
AUC
****
****
High EGF
Low EGF
MCUi11/ High
F
High EGF
Control
RTN3 KD
RTN4 KD
MCU KD
IP3R KD
Mito-GCaMP6m 490/406
time (sec)
AUC
****
ns
****
****
Control
RTN3 KD
RTN4 KD
IP3R KD
MCU KD

Figure 2

Fig. 2. EGFR-NCE induces Ca^{2+} oscillations at the PM which rely on mitochondrial Ca^{2+} buffering activity. (**A**) Schematic of the GCaMP6f Ca^{2+} probe targeted to the PM inner leaflet (PM-GCaMP6f, left) or to inside mitochondria (mito-GCaMP6m, right). (**B**) HeLa PM-GCaMP6f cells were stimulated with low dose EGF (N=17) or high dose EGF in the presence of RTN3 KD (N=25), RTN4 KD (N=26) or IP3R KD (N=25) or mock control (N=40) and fluorescence monitored. Results (here and in panels C-F) are presented as the ratio of the emission at 490/406 nm. Left, representative single cell response curves. Right, mean AUC ± SD. N=number of cells (all panels); n=3. (**C-D**) HeLa PM-GCaMP6f cells subjected or not to MCU KD (C) or MCUi11 treatment (D) and stimulated with high dose EGF. (C) Control N=44; MCU KD N=21 (n=4); (D) Control N=20; MCUi11 treated N=20 (n=2). (**E**) HeLa mito-GCaMP6m cells treated with low EGF (N=10) or high EGF alone (N=27) or with MCUi11 (N=30); n=1. (**F**) HeLa mito-GCaMP6m cells subjected or not to the indicated KDs and stimulated with high dose EGF. Control N=123; RTN3 KD N=135; RTN4 KD N=95; IP3R KD N=123; MCU KD N=101 (n=4).

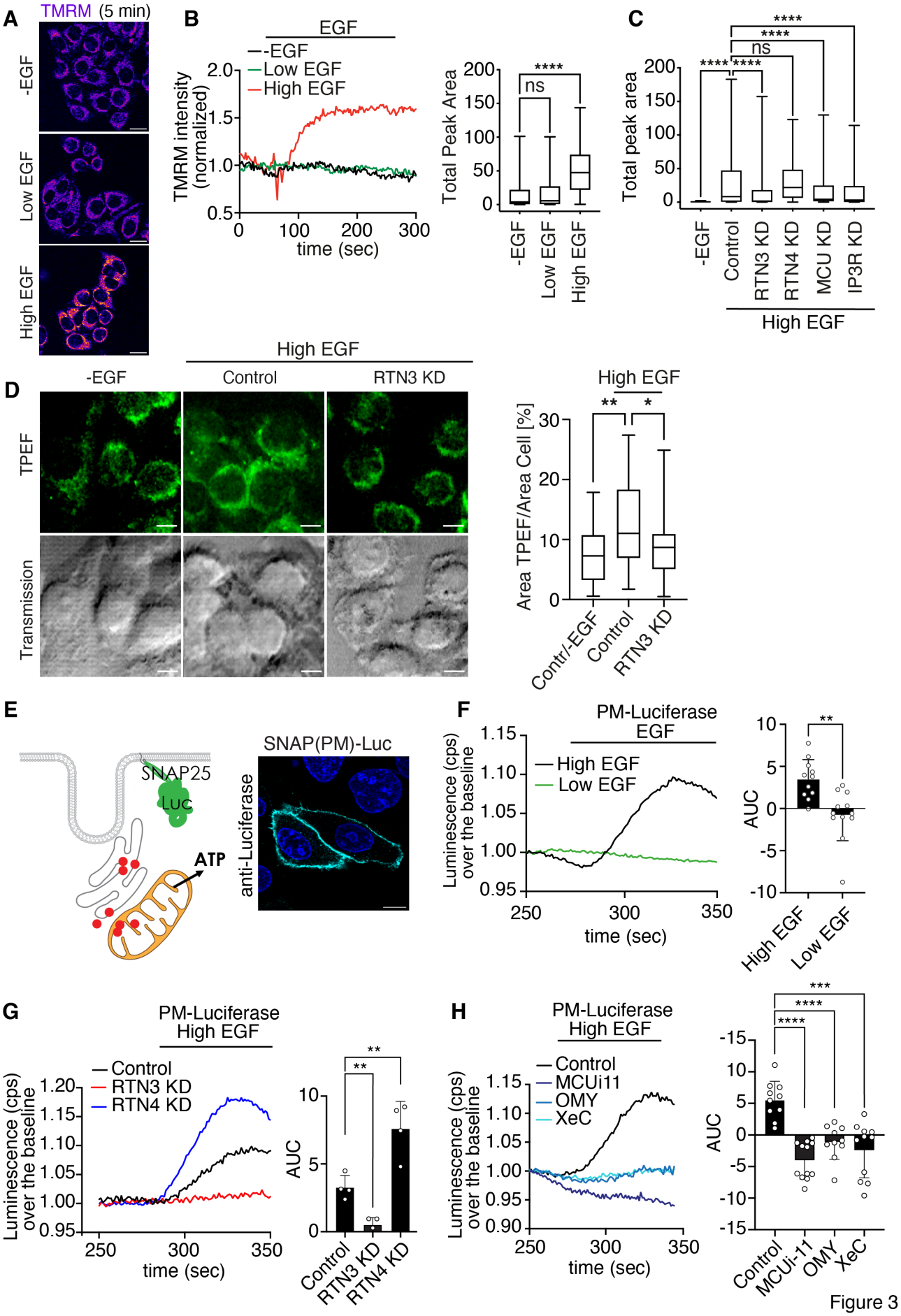

Figure 3

Fig. 3. NCE-associated Ca^{2+} oscillations induce mitochondrial ATP production. (**A**) Representative images of TMRM fluorescence in HeLa cells stimulated or not with low or high dose EGF after 45 sec since recording started. Bar, 10 µM. (**B**) Left, time course of TMRM fluorescence intensity in cells treated as in "A". Right, Total peak area ± SD; -EGF N=219; Low EGF N=217; High EGF N=205; N=number of cells; n=5. (**C**) TMRM fluorescence measured in HeLa cells, subjected to the indicated KD or mock control, and stimulated with high dose EGF for 5 min. Mock unstimulated cells (-EGF) served as the negative control. Total peak area ± SD is reported. N=number of cells: -EGF N=41, Control N=421, RTN3 KD N=316, RTN4 KD N=324, IP3R KD N=265, IP3R KD N=228 (n=3). (**D**) Left, representative TPEF images of mock transfected HeLa cells left unstimulated (-EGF) or HeLa cells subjected to RTN3 KD or mock transfection (Control) and stimulated with high dose EGF for 5 min. Images have a dimension of 70x70 μm^2. Scale bar: 10 µm. Right, quantification of the distribution of the TPEF signal in HeLa cells treated as in left panel: -EGF N=130, Control/High EGF=160, RTN3 KD/High EGF=135 (n=3). Statistical significance was calculated using the non-parametric U-Mann Whitney test. (**E**) Left, schematic showing luciferase targeted to the PM inner leaflet by fusion with the PM-targeting domain of SNAP25. Right, IF staining showing the localization of the SNAP25-luciferase fusion protein [SNAP(PM)-Luc]. Bar, 10 µm. (**F**) Luminescence was measured in HeLa cells expressing PM-Luc stimulated with low or high EGF. Left, representative curves of luminescence over the baseline; cps, count per second. Right, mean AUC ± SD. N=number of coverslips (for panels F-H): High EGF N=11, Low EGF N=12 (n=2). (**G-H**) Luminescence was measured in HeLa cells expressing PM-Luc were subjected or not to the indicated KDs (G) or inhibitor treatments (H) and stimulated with high dose EGF. Results are presented as in (F). (G) Control N=4, RTN3 KD N=4, RTN4 KD N=4 (n=4): a representative experiment is shown. (H) Control N=10, MCUi11 N=12, oligomycin (OMY) N=10, xestospongin (XeC) N=11 (n=3).

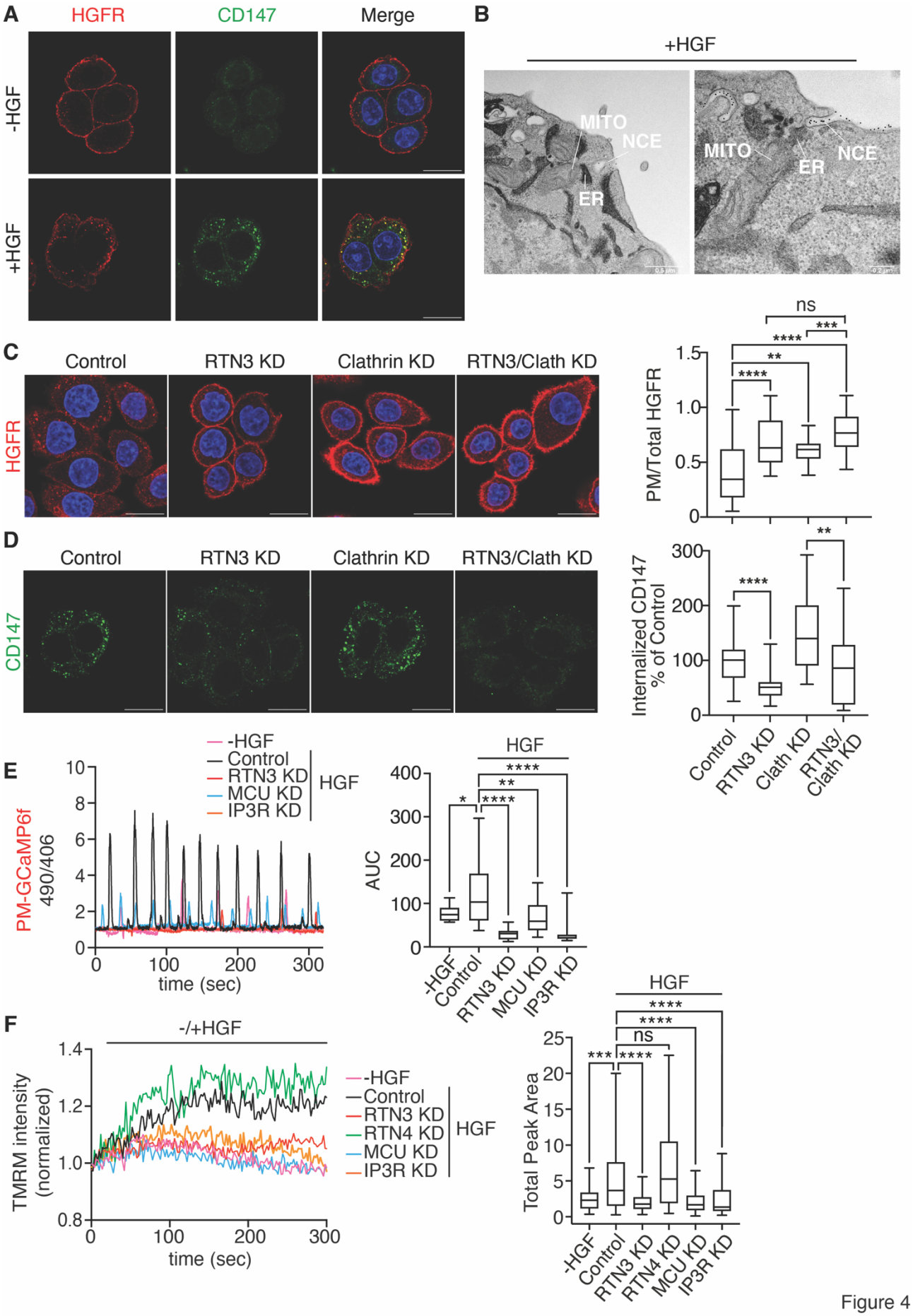

Figure 4

Fig. 4. HGFR is internalized via NCE and relies on the same Ca^{2+}/ATP circuitry as EGFR.

(**A**) Representative immuno-electron microscopy image of CD147-positive NCE structures in contact with the ER, which is, in turn, in contact with a mitochondrion. HeLa cells were stimulated with HGF (100 ng/ml) for 5 min at 37°C. CD147 was immunolabelled with gold. The ER was stained with HRP-KDEL. Bar, 0.25 µM. (**B**) CD147 internalization was monitored *in vivo* in HeLa cells. Cells were incubated with an anti-CD147 antibody and an Alexa-488 secondary antibody (green) prior to stimulation with HGF (100 ng/ml) for 8 min. Control cells were left unstimulated. Acid wash treatment was applied prior to fixation. HGFR was stained with a specific antibody after fixation and permeabilization (red). Representative IF images are shown. Blue, DAPI. Bar, 20 µm. (**C**) HGFR internalization was quantified in HeLa cells under different KD conditions, following the same procedure as described in section "A". After fixation, HGFR was stained with a primary antibody followed by CY3-labelled secondary antibody to detect PM HGFR prior to permeabilization. Cells were then further fixed and permeabilized to enable staining of total HGFR by staining with primary antibody followed by Alexa 647-labelled secondary. Representative IF images of total HGFR are shown on the left. Bar, 20 µm. Image analysis was performed using ImageJ software. Quantification of the ratio of PM HGFR to total HGFR is shown on the right. (**D**) CD147 internalization in HeLa cells was quantified under different KD conditions, following the same procedure as described in "A". The mean integrated fluorescence intensity is expressed as a percentage of control ± SD. The number of cells (N) for each condition: Control N=94, RTN3 KD N=105, Clathrin KD N=111, RTN3/Clathrin KD N=94; for HGFR, Control N=114, RTN3 KD N=130, Clathrin KD N=126, RTN3/Clathrin KD N=122 (n=2). (**E**) HeLa PM-GCaMP6f cells were subjected to the indicated KDs or a mock control, and stimulated with HGF (250 ng/ml) or left unstimulated. Fluorescence was monitored, and the results are presented as the ratio of emission at 490/406 nm. Left, representative single cell response curves. Right, mean area under the curve (AUC) ± SD. EGF N=10, Control N=37, RTN3 KD N=32, MCU KD N=30, IP3R KD N=30 (n=1). (**F**) TMRM fluorescence was measured in HeLa cells subjected to the indicated KDs or a mock control and stimulated with HGF (100 ng/ml) for 5 min after a 45-sec recording period. Mock unstimulated cells (-HGF) were used as the negative control. Left, representative traces. Right, total peak area ± SD is reported. -EGF N=57, Control N=223, RTN3 KD N=229, RTN4 KD N=162, MCU KD N=310, IP3R KD N=219 (n=1).

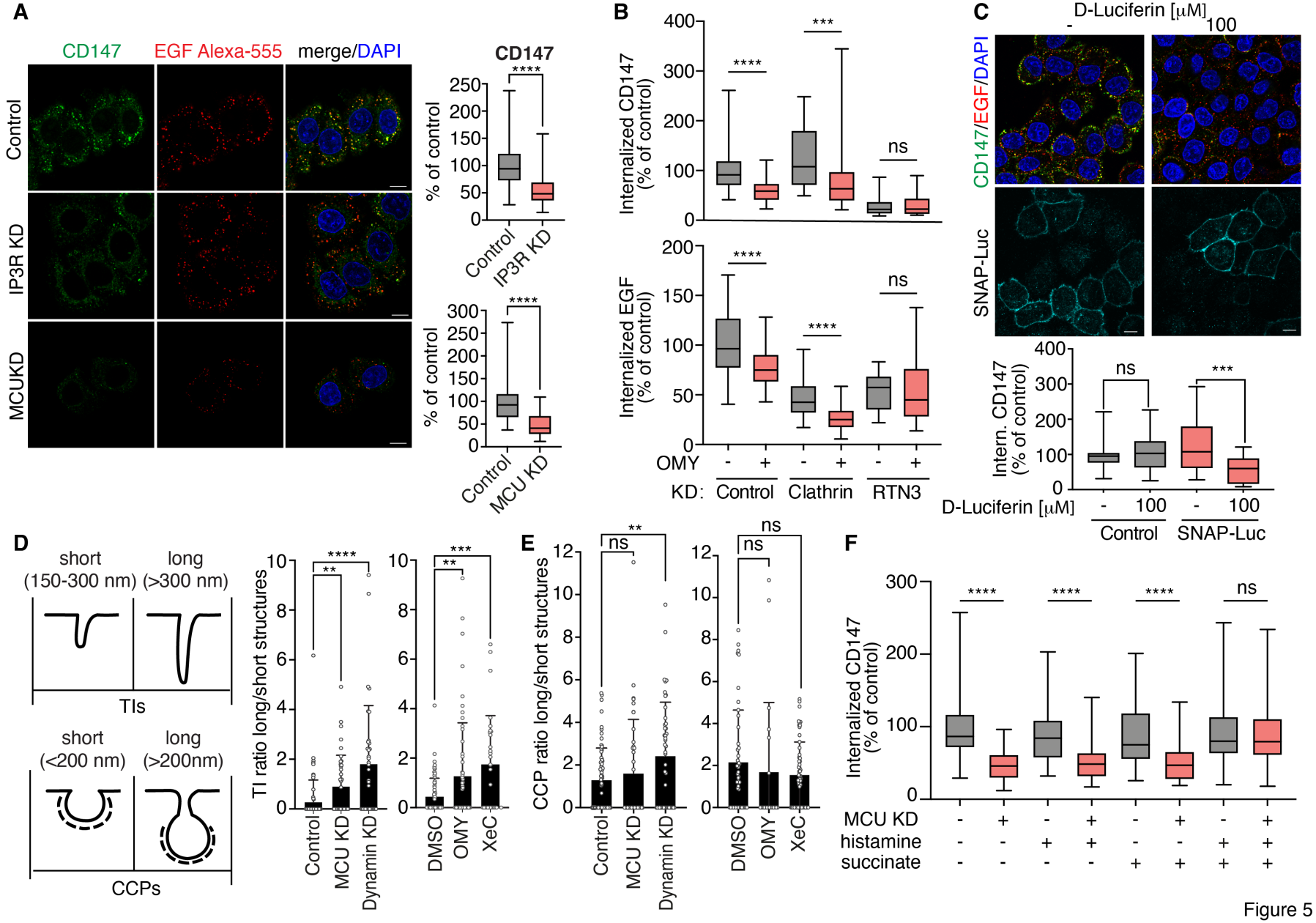
A
CD147
EGF Alexa-555
merge/DAPI
Control
IP3R KD
MCUKD
CD147
% of control
Control
IP3R KD
MCU KD
B
Internalized CD147 (% of control)
Internalized EGF (% of control)
OMY
KD: Control
Clathrin
RTN3
C
D-Luciferin [μM]
CD147/EGF/DAPI
SNAP-Luc
Intern. CD147 (% of control)
Control
SNAP-Luc
D
short (150-300 nm)
long (>300 nm)
TIs
short (<200 nm)
long (>200nm)
CCPs
TI ratio long/short structures
DMSO
OMY
XeC
E
CCP ratio long/short structures
F
Internalized CD147 (% of control)
MCU KD
histamine
succinate

Figure 5

Fig. 5. EGF-induced Ca^{2+} waves and mitochondrial ATP production are required for NCE execution. (**A**) CD147 internalization was monitored *in vivo* by IF in HeLa cells subjected to the indicated KDs or mock control and stimulated with high dose Alexa-555 EGF. Cells were subjected to acid wash prior to fixation to remove membrane-bound antibodies and analyzed by confocal microscopy. Left, representative IF images, Blue, DAPI. Bar, 10 µm. Right, quantification of CD147 fluorescence intensity expressed as % of control ± SD. N=number of cells: Control N=699 (n=8); IP3R KD N=673 (n=8); Control N=258 (n=5); MCU KD N=239 (n=5). (**B**) Internalization of CD147 and Alexa-555 EGF was monitored as in (A) in HeLa cells subjected to the indicated KDs and treated or not with OMY (1 µM, pretreatment for 5 min). CD147 and Alexa-555 EGF fluorescence intensity is expressed as % of control ± SD. N=number of cells: Control N=222 (n=4); Control+OMY N=217 (n=4); Clathrin KD N=201 (n=4); Clathrin KD+OMY N=252 (n=4); RTN3 KD N=106 (n=2); RTN3 KD+OMY N=132 (n=4). (**C**) HeLa cells were transfected with PM-Luc and treated or not with luciferin (100 µM). CD147 internalization was monitored as in (A). Top, representative IF images, Blue, DAPI. Bar, 10 µm. Bottom, quantification of CD147 fluorescence intensity expressed as % of control ± SD. N=number of cells: Control N=158, Control+Luciferin N=142, n=3; SNAP-Luc N=116, SNAP-Luc+Luciferin N=78, n=4. (**D, E**) EM morphometric analysis of the length of EGFR gold-positive TIs or CCPs in HeLa cells subjected to the indicated KDs or drug treatments. (D) Left, schematic representation of the criteria used to assign TIs or CCPs as short or long. Right, quantification of the ratio of long *vs.* short NCE TIs normalized to PM profiles of 100 µm length. N=cell profiles: Control N=70, MCU KD N=39, Dynamin KD N=35 (n=2); DMSO N=71, OMY N=56 (n=3); XeC N=20 (n=2). (E) Quantification of the ratio of long *vs.* short CCPs normalized to PM profiles of 100 µm length. N=cell profiles: Control N=70 (n=3); MCU KD N=39 (n=2); Dynamin KD N=45 (n=3); DMSO N=45 (n=3); OMY N=56 (n=3); XeC N=20 (n=2). (**F**) HeLa cells were subjected to MCU KD or mock control and treated or not with histamine and/or succinate as indicated. CD147 internalization was monitored *in vivo* as in "A". Quantification of CD147 fluorescence intensity expressed as % of control ± SD. N=number of cells: Control N=281, MCU KD N=345, Histamine N=177, MCU KD+Histamine N=264, Succinate N=169, MCU KD+Succinate N=202, Histamine/Succinate N=225, MCU KD+Histamine/Succinate N=241 (n=3).

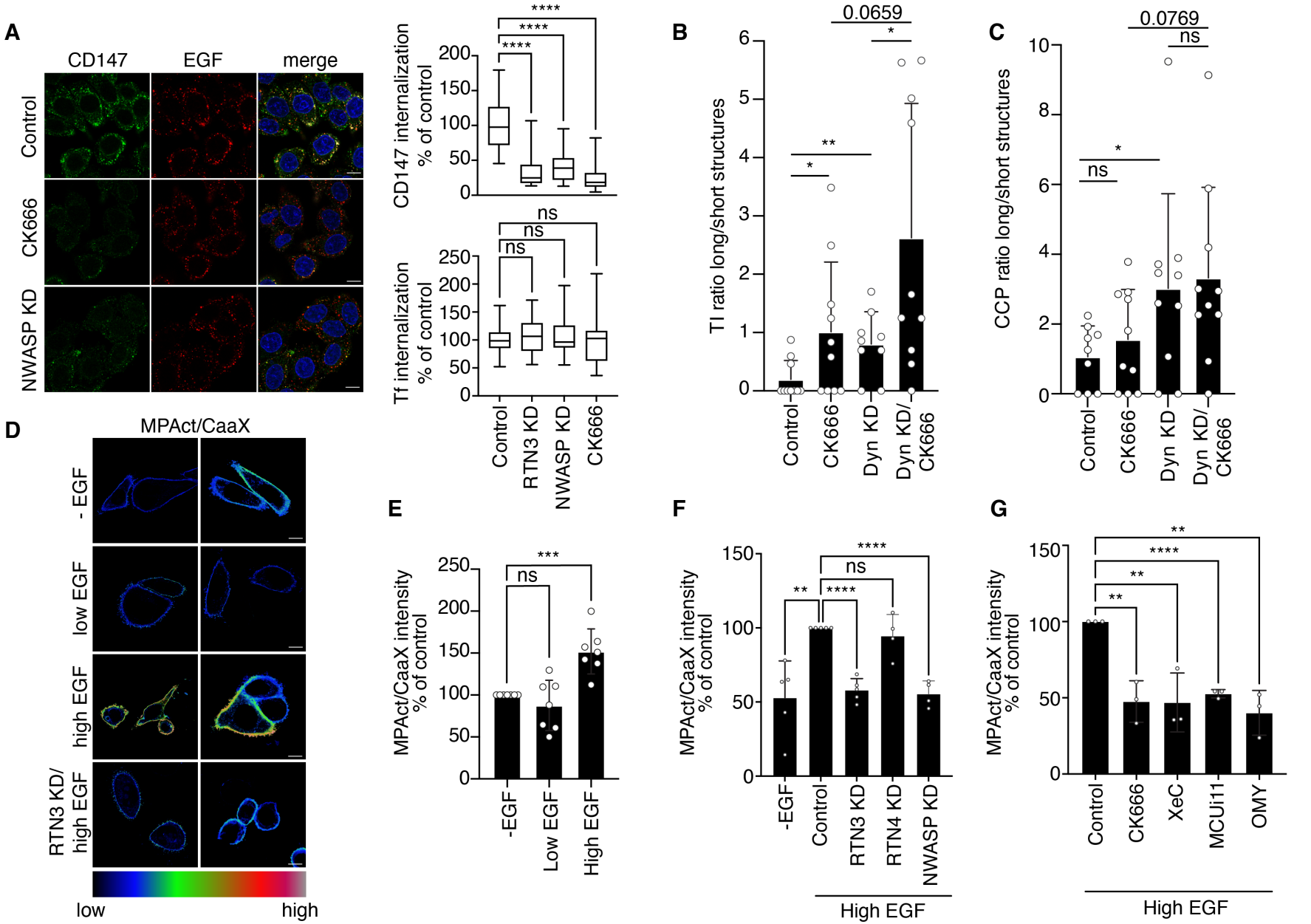
A
CD147
EGF
merge
Control
CK666
NWASP KD
CD147 internalization
% of control
Tf internalization
% of control
Control
RTN3 KD
NWASP KD
CK666
B
TI ratio long/short structures
0.0659
Control
CK666
Dyn KD
Dyn KD/
CK666
C
CCP ratio long/short structures
0.0769
ns
D
MPAct/CaaX
- EGF
low EGF
high EGF
RTN3 KD/
high EGF
low
high
E
MPAct/CaaX intensity
% of control
-EGF
Low EGF
High EGF
F
MPAct/CaaX intensity
% of control
-EGF
Control
RTN3 KD
RTN4 KD
NWASP KD
High EGF
G
MPAct/CaaX intensity
% of control
Control
CK666
XeC
MCUi11
OMY
High EGF

Figure 6

Fig. 6. Ca^{2+} and ATP are required for cortical actin cytoskeleton remodeling which is involved in the fission of NCE TIs. (**A**) CD147 internalization was monitored in HeLa cells subjected to N-WASP KD or treatment with CK666 and stimulated with high dose EGF. RTN3 KD was used as a positive control for NCE inhibition. Left, representative IF images, CD147 (green), EGF (red), DAPI (blue), Bar, 10 µm. Right upper, quantification of relative CD147 fluorescence intensity expressed as % of control ± SD. N=number of cells: Control N=258, RTN3 KD N=73, NWASP KD N=231, CK666 N=242 (n=3). Right lower, Alexa647-Tf internalization was monitored for 8 min at 37°C in HeLa cells treated as above. The data reported for RTN3 KD are the same as displayed in Fig. 4B. N=number of cells: Control N=246, RTN3 KD N=185, NWASP KD N=276, CK666 N=295 (n=3). (**B, C**) EM morphometric analysis of the length of EGFR gold-positive TIs (B) and CCPs (C) in HeLa cells subjected to dynamin KD (Dyn KD) and/or treated with CK666. Data are expressed as the ratio between the number of long to short structures (as defined in Fig. 4D) normalized to PM profiles of 100 µm length; N=cell profiles. Control N=10, CK666 N=10, Dyn KD N=9, Dyn KD/CK666 N=10 (B); Control N=9, CK666 N=10, Dyn KD N=10, Dyn KD/CK666 N=10 (C); a representative experiment of two biological replicates is shown. (**D**) Ratiometric analysis of membrane proximal actin (MPA) density. HeLa cells were subjected or not to RTN3 KD, followed by MPAct-mCherry and YFP-CaaX co-transfection, and then stimulated with high or low EGF or left unstimulated (-EGF). Left, two representative images of the ratiometric analysis of MPA density where the MPAct signal is normalized over the CaaX PM marker. (**E**) Right, mean raw integrated fluorescence intensity ± SD is reported as a percentage relative to control cells. N=number of cells: -EGF N=424, Low EGF N=495, High EGF N=568 (n=7). (**F,G**) Ratiometric analysis of MPA density as in (D), in HeLa cells subjected to the indicated KDs (F) or inhibitor treatments (G) and stimulated with high dose EGF. Inhibitors were present during the stimulation. N=number of cells: (F) -EGF N=316 (n=5), Control N=356 (n=5), RTN3 KD N=409 (n=5), RTN4 KD N=311 (n=4), NWASP KD N=370 (n=4); (G) Control N=306, CK666 N=228, XeC N=231, MCUi11 N=232, OMY N=189 (n=3).

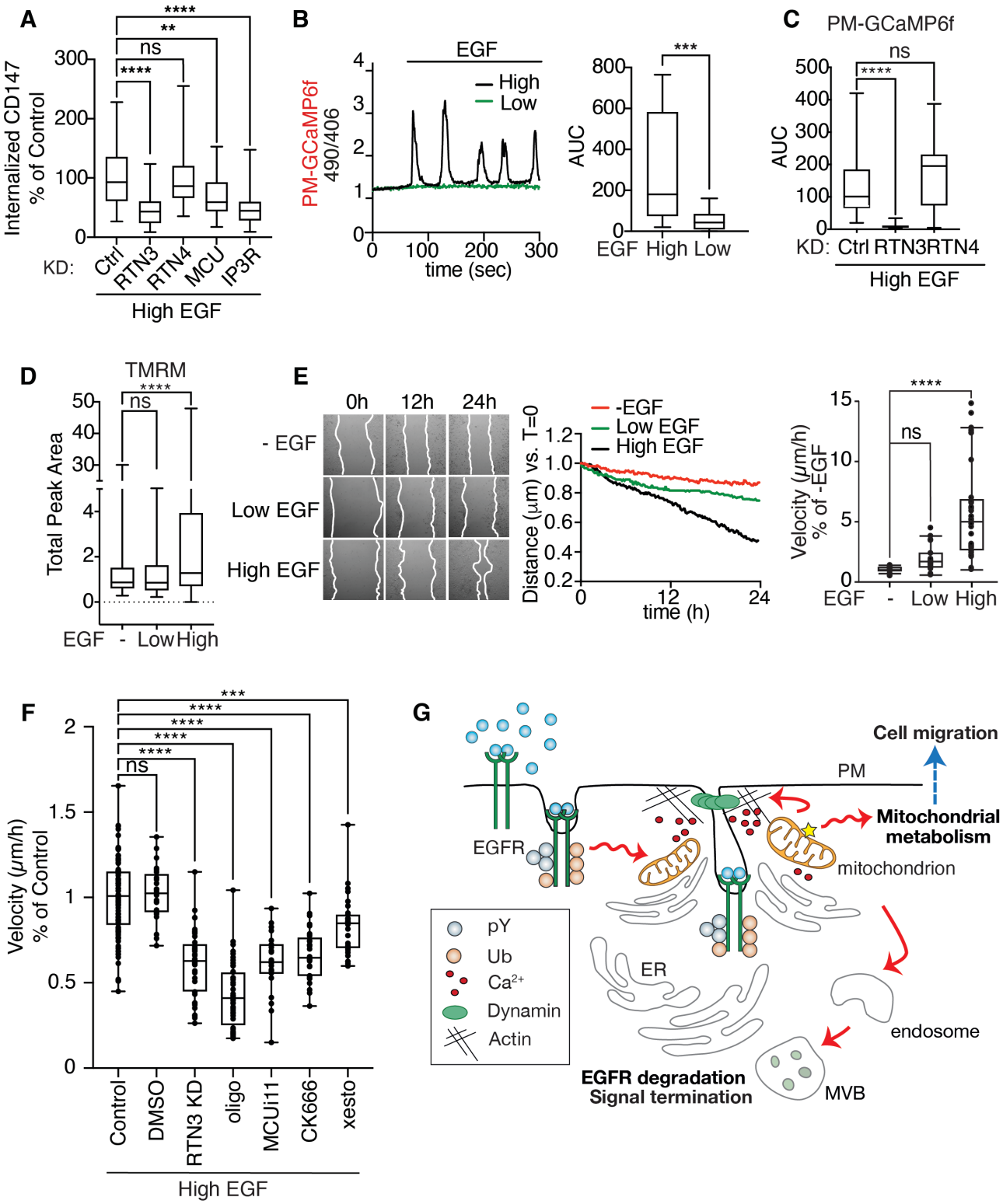

Figure 7

Fig. 7. The EGFR-NCE multiorganelle platform mediates EGF-induced migration in keratinocytes. (**A**) CD147 internalization in HaCaT cells subjected to the indicated KDs or mock transfection (Ctrl). Internalized CD147 was measured by IF after stimulation with high dose Alexa647-EGF for 12 min at 37°C, as described in Fig. 4A. Mean integrated fluorescence intensity

± SD is reported as a percentage of the control cells. N=number of cells: Control N=301 (n=6), RTN3 KD N=97 (n=3), RTN4 KD N=179 (n=5), MCU KD N=253 (n=5), IP3R KD N=199 (n=4). (**B**) HaCaT cells expressing the Ca^{2+} sensor PM-GCaMP6f were stimulated with high or low EGF. Left, Representative single-cell Ca^{2+} response curves presented as the ratio of fluorescence emission at 490/406 nm. Right, AUC ± SD of the Ca^{2+} response. N=number of cells: High EGF N=17, Low EGF N=20 (n=3). (**C**) Ca^{2+} response in HaCaT cells subjected to RTN3 or RTN4 KD or to mock transfection (Ctrl) and stimulated with high EGF dose as in (B). AUC ± SD is shown. N=number of cells: Control N=18, RTN3 KD N=27, RTN4 KD N=14. A representative experiment of three independent replicates is shown. (**D**) ΔΨm in HaCaT cells stimulated or not with low or high EGF, measured using TMRM. Total peak area ± SD is reported. N=number of cells: -EGF N=206, Low EGF N=253, High EGF N=327. A representative experiment of two independent replicates is shown. (**E**) Wound healing in sub-confluent HaCaT cells stimulated or not with low or high EGF was monitored by time-lapse video microscopy. Left, representative images at the indicated time points. Middle, distance covered by cells in the different conditions corrected to the baseline at t=0. Right, wound closure velocity (μm/h) at t=24 h is shown. N=number of cells: -EGF N=15, Low EGF N=23, High EGF N=34 (n=3). (**F**) Wound closure velocity (μm/h) in sub-confluent HaCaT cells stimulated with high EGF dose and subjected to RTN3 KD or the indicated treatments for 24 h. N=number of cells: Control N=121 (n=3), DMSO N=24 (n=2), RTN3 KD N=40 (n=2), OMY N=44 (n=3), MCUi11 N=22 (n=2), CK666 N=28 (n=2), XeC N=30 (n=2). **G.** Schematic showing the crosstalk between EGFR-NCE, ER and mitochondria in controlling EGFR endocytosis, receptor fate and cell migration.

References

1. Burgess, A.W. Regulation of Signaling from the Epidermal Growth Factor Family. *J Phys Chem B* **126**, 7475-7485 (2022).
2. Lemmon, M.A., Schlessinger, J. & Ferguson, K.M. The EGFR family: not so prototypical receptor tyrosine kinases. *Cold Spring Harb Perspect Biol* **6**, a020768 (2014).
3. Freed, D.M. *et al.* EGFR Ligands Differentially Stabilize Receptor Dimers to Specify Signaling Kinetics. *Cell* **171**, 683-695 e618 (2017).
4. Wilson, K.J., Gilmore, J.L., Foley, J., Lemmon, M.A. & Riese, D.J., 2nd Functional selectivity of EGF family peptide growth factors: implications for cancer. *Pharmacol Ther* **122**, 1-8 (2009).
5. Caldieri, G. *et al.* Reticulon 3-dependent ER-PM contact sites control EGFR nonclathrin endocytosis. *Science* **356**, 617-624 (2017).
6. Sigismund, S. *et al.* Clathrin-independent endocytosis of ubiquitinated cargos. *Proc Natl Acad Sci U S A* **102**, 2760-2765 (2005).
7. Sigismund, S. *et al.* Threshold-controlled ubiquitination of the EGFR directs receptor fate. *EMBO J* **32**, 2140-2157 (2013).
8. Sigismund, S. *et al.* Clathrin-mediated internalization is essential for sustained EGFR signaling but dispensable for degradation. *Dev Cell* **15**, 209-219 (2008).

9. Wu, H. & Voeltz, G.K. Reticulon-3 Promotes Endosome Maturation at ER Membrane Contact Sites. *Dev Cell* **56**, 52-66 e57 (2021).
10. Grumati, P. *et al.* Full length RTN3 regulates turnover of tubular endoplasmic reticulum via selective autophagy. *Elife* **6** (2017).
11. Jang, W. *et al.* Endosomal lipid signaling reshapes the endoplasmic reticulum to control mitochondrial function. *Science* **378**, eabq5209 (2022).
12. Chen, T.W. *et al.* Ultrasensitive fluorescent proteins for imaging neuronal activity. *Nature* **499**, 295-300 (2013).
13. Gaspers, L.D. *et al.* Hormone-induced calcium oscillations depend on cross-coupling with inositol 1,4,5-trisphosphate oscillations. *Cell Rep* **9**, 1209-1218 (2014).
14. Rizzuto, R., Simpson, A.W., Brini, M. & Pozzan, T. Rapid changes of mitochondrial Ca2+ revealed by specifically targeted recombinant aequorin. *Nature* **358**, 325-327 (1992).
15. Baughman, J.M. *et al.* Integrative genomics identifies MCU as an essential component of the mitochondrial calcium uniporter. *Nature* **476**, 341-345 (2011).
16. Bonora, M. *et al.* Comprehensive analysis of mitochondrial permeability transition pore activity in living cells using fluorescence-imaging-based techniques. *Nat Protoc* **11**, 1067-1080 (2016).
17. Di Marco, G. *et al.* A High-Throughput Screening Identifies MICU1 Targeting Compounds. *Cell Rep* **30**, 2321-2331 e2326 (2020).
18. De Stefani, D., Raffaello, A., Teardo, E., Szabo, I. & Rizzuto, R. A forty-kilodalton protein of the inner membrane is the mitochondrial calcium uniporter. *Nature* **476**, 336-340 (2011).
19. Bonora, M. *et al.* Subcellular calcium measurements in mammalian cells using jellyfish photoprotein aequorin-based probes. *Nat Protoc* **8**, 2105-2118 (2013).
20. Bonora, M. *et al.* ATP synthesis and storage. *Purinergic Signal* **8**, 343-357 (2012).
21. Scaduto, R.C., Jr. & Grotyohann, L.W. Measurement of mitochondrial membrane potential using fluorescent rhodamine derivatives. *Biophys J* **76**, 469-477 (1999).
22. Liu, Z. *et al.* Mapping metabolic changes by noninvasive, multiparametric, high-resolution imaging using endogenous contrast. *Sci Adv* **4**, eaap9302 (2018).
23. Talone, B. *et al.* Label-free multimodal nonlinear optical microscopy reveals features of bone composition in pathophysiological conditions. *Front Bioeng Biotechnol* **10**, 1042680 (2022).
24. Jouaville, L.S., Pinton, P., Bastianutto, C., Rutter, G.A. & Rizzuto, R. Regulation of mitochondrial ATP synthesis by calcium: evidence for a long-term metabolic priming. *Proc Natl Acad Sci U S A* **96**, 13807-13812 (1999).
25. Barrow-McGee, R. & Kermorgant, S. Met endosomal signalling: in the right place, at the right time. *Int J Biochem Cell Biol* **49**, 69-74 (2014).
26. Abella, J.V. *et al.* Met/Hepatocyte growth factor receptor ubiquitination suppresses transformation and is required for Hrs phosphorylation. *Mol Cell Biol* **25**, 9632-9645 (2005).
27. Petrelli, A. *et al.* The endophilin-CIN85-Cbl complex mediates ligand-dependent downregulation of c-Met. *Nature* **416**, 187-190 (2002).
28. Antonny, B. *et al.* Membrane fission by dynamin: what we know and what we need to know. *EMBO J* **35**, 2270-2284 (2016).
29. McCullagh, M., Saunders, M.G. & Voth, G.A. Unraveling the mystery of ATP hydrolysis in actin filaments. *J Am Chem Soc* **136**, 13053-13058 (2014).
30. Pollard, T.D. Actin and Actin-Binding Proteins. *Cold Spring Harb Perspect Biol* **8** (2016).
31. Carlier, M.F. *et al.* Control of polarized assembly of actin filaments in cell motility. *Cell Mol Life Sci* **72**, 3051-3067 (2015).
32. Boulant, S., Kural, C., Zeeh, J.C., Ubelmann, F. & Kirchhausen, T. Actin dynamics counteract membrane tension during clathrin-mediated endocytosis. *Nat Cell Biol* **13**, 1124-1131 (2011).
33. Hinze, C. & Boucrot, E. Local actin polymerization during endocytic carrier formation. *Biochem Soc Trans* **46**, 565-576 (2018).

34. Bretscher, M.S. & Aguado-Velasco, C. EGF induces recycling membrane to form ruffles. *Curr Biol* **8**, 721-724 (1998).
35. Bisaria, A., Hayer, A., Garbett, D., Cohen, D. & Meyer, T. Membrane-proximal F-actin restricts local membrane protrusions and directs cell migration. *Science* **368**, 1205-1210 (2020).
36. Palamidessi, A. *et al.* Unjamming overcomes kinetic and proliferation arrest in terminally differentiated cells and promotes collective motility of carcinoma. *Nat Mater* **18**, 1252-1263 (2019).
37. Koivisto, L., Jiang, G., Hakkinen, L., Chan, B. & Larjava, H. HaCaT keratinocyte migration is dependent on epidermal growth factor receptor signaling and glycogen synthase kinase-3alpha. *Exp Cell Res* **312**, 2791-2805 (2006).
38. Janikiewicz, J. *et al.* Mitochondria-associated membranes in aging and senescence: structure, function, and dynamics. *Cell Death Dis* **9**, 332 (2018).
39. Scorrano, L. *et al.* Coming together to define membrane contact sites. *Nat Commun* **10**, 1287 (2019).
40. Venditti, R., Wilson, C. & De Matteis, M.A. Regulation and physiology of membrane contact sites. *Curr Opin Cell Biol* **71**, 148-157 (2021).
41. Prinz, W.A., Toulmay, A. & Balla, T. The functional universe of membrane contact sites. *Nat Rev Mol Cell Biol* **21**, 7-24 (2020).
42. Carpenter, G. & Cohen, S. Human epidermal growth factor and the proliferation of human fibroblasts. *J Cell Physiol* **88**, 227-237 (1976).
43. Di Fiore, P.P. *et al.* Overexpression of the human EGF receptor confers an EGF-dependent transformed phenotype to NIH 3T3 cells. *Cell* **51**, 1063-1070 (1987).
44. Das, M. & Fox, C.F. Molecular mechanism of mitogen action: processing of receptor induced by epidermal growth factor. *Proc Natl Acad Sci U S A* **75**, 2644-2648 (1978).
45. Lang, E. *et al.* Coordinated collective migration and asymmetric cell division in confluent human keratinocytes without wounding. *Nat Commun* **9**, 3665 (2018).
46. Goetz, J.G. *et al.* Reversible interactions between smooth domains of the endoplasmic reticulum and mitochondria are regulated by physiological cytosolic Ca2+ levels. *J Cell Sci* **120**, 3553-3564 (2007).
47. Wang, H.J., Guay, G., Pogan, L., Sauve, R. & Nabi, I.R. Calcium regulates the association between mitochondria and a smooth subdomain of the endoplasmic reticulum. *J Cell Biol* **150**, 1489-1498 (2000).
48. Hajnoczky, G. & Thomas, A.P. Minimal requirements for calcium oscillations driven by the IP3 receptor. *EMBO J* **16**, 3533-3543 (1997).
49. Kirchhausen, T. Bending membranes. *Nat Cell Biol* **14**, 906-908 (2012).
50. Sackmann, E. The seventh Datta Lecture. Membrane bending energy concept of vesicle- and cell-shapes and shape-transitions. *FEBS Lett* **346**, 3-16 (1994).
51. Dannhauser, P.N. & Ungewickell, E.J. Reconstitution of clathrin-coated bud and vesicle formation with minimal components. *Nat Cell Biol* **14**, 634-639 (2012).
52. Tosatto, A. *et al.* The mitochondrial calcium uniporter regulates breast cancer progression via HIF-1alpha. *EMBO Mol Med* **8**, 569-585 (2016).
53. Prudent, J. *et al.* Mitochondrial Ca(2+) uptake controls actin cytoskeleton dynamics during cell migration. *Sci Rep* **6**, 36570 (2016).
54. Stejerean-Todoran, I. *et al.* MCU controls melanoma progression through a redox-controlled phenotype switch. *EMBO Rep* **23**, e54746 (2022).
55. Schwarz, T.L. Mitochondrial trafficking in neurons. *Cold Spring Harb Perspect Biol* **5** (2013).
56. Soubannier, V. & McBride, H.M. Positioning mitochondrial plasticity within cellular signaling cascades. *Biochim Biophys Acta* **1793**, 154-170 (2009).

57. Cunniff, B., McKenzie, A.J., Heintz, N.H. & Howe, A.K. AMPK activity regulates trafficking of mitochondria to the leading edge during cell migration and matrix invasion. *Mol Biol Cell* **27**, 2662-2674 (2016).
58. Desai, S.P., Bhatia, S.N., Toner, M. & Irimia, D. Mitochondrial localization and the persistent migration of epithelial cancer cells. *Biophys J* **104**, 2077-2088 (2013).
59. Rivadeneira, D.B. *et al.* Survivin promotes oxidative phosphorylation, subcellular mitochondrial repositioning, and tumor cell invasion. *Sci Signal* **8**, ra80 (2015).
60. Schuler, M.H. *et al.* Miro1-mediated mitochondrial positioning shapes intracellular energy gradients required for cell migration. *Mol Biol Cell* **28**, 2159-2169 (2017).
61. Shin, K.J. *et al.* A single lentiviral vector platform for microRNA-based conditional RNA interference and coordinated transgene expression. *Proc Natl Acad Sci U S A* **103**, 13759-13764 (2006).
62. Patron, M. *et al.* MICU1 and MICU2 finely tune the mitochondrial Ca2+ uniporter by exerting opposite effects on MCU activity. *Mol Cell* **53**, 726-737 (2014).
63. Schikorski, T., Young, S.M., Jr. & Hu, Y. Horseradish peroxidase cDNA as a marker for electron microscopy in neurons. *J Neurosci Methods* **165**, 210-215 (2007).
64. Bolte, S. & Cordelieres, F.P. A guided tour into subcellular colocalization analysis in light microscopy. *J Microsc* **224**, 213-232 (2006).
65. Morciano, G. *et al.* Use of luciferase probes to measure ATP in living cells and animals. *Nat Protoc* **12**, 1542-1562 (2017).
66. Parodi, V. *et al.* Characterization of Mesenchymal Stem Cell Differentiation within Miniaturized 3D Scaffolds through Advanced Microscopy Techniques. *Int J Mol Sci* **21** (2020).

MATERIALS AND METHODS

EGF concentrations and reagents

Throughout the manuscript low and high dose EGF means 1 and 100 ng/ml, respectively. Alexa-labeled EGF was used at a concentration of 1 µg/ml of the conjugated species, corresponding to an actual EGF concentration of ~40 ng/ml. EGF was from PeproTech; Alexa-EGF and Alexa-Tf were from Molecular Probes. Purified human recombinant HGF (100-250 ng/ml, as indicated) was obtained from R&D Systems. Protein-A Gold 10 nm was from Utrecht University; EM grade glutaraldehyde and paraformaldehyde were from Electron Microscopy Sciences; ruthenium red and secondary rabbit anti-mouse were from Sigma. Fluorescent secondary antibodies were from Jackson ImmunoResearch. Beetle Luciferin Potassium Salt for Luciferase-based assays was from Promega. Oligomycin (OMY), histamine and succinate were from Sigma, xestospongin C (XeC) was from abcam, CK666 and bongkrekic acid were from Merck Life Technology S.R.L., and MCUi11 was from CliniSciences.

Drug treatments

Cells were treated with 20 µM XeC for 30 min (except for the wound-healing assay where it was used at 2 µM for 24 h), 50 µM CK666 for 1 h, 1 µM OMY for 15 min (except for the PM-Luc assay where it was used at 10 µM for 40 min), 50 µM MCUi11 for 30 min, 50 µM bongkrekic Acid for 15 min. The drugs were kept for the duration of the different experimental procedures (CD147 internalization followed by EM/IF analysis, TMRM live recording, PM-Luc ATP recording, MPAct/CaaX actin polymerization).

Constructs

pGP-CMV-GCaMP6f was a gift from Douglas Kim & GENIE Project (Addgene plasmid # 40755; http://n2t.net/addgene:40755; RRID:Addgene 40755). For the SNAP25-GCaMP6f tagged version, the SNAP25-Aequorin sequence was used as a template for the PCR reaction. To generate PM-Luc stably expressing clones, SNAP25 tag was subcloned from SNAP25-GCaMP6f in the pcDNA3.1 vector (Invitrogen) by PCR using XHOI and BAMHI restriction enzymes. Luciferase cDNA was subcloned by PCR from the CytLuc-pGL3 basic plasmid into the SNAP25-pcDNA3 vector via Nebuilder Hifi DNA Assembly Cloning Kit using the XHOI restriction enzyme. Then, SNAP25-luciferase cDNA was subcloned into the pLVX-Puro vector (Clonetech) using the NEBuilder HiFi DNA Assembly Cloning Kit and the BAMHI restriction enzyme. To generate the PM-GCaMP6f stably expressing HeLa and HaCaT clones, the SNAP25-GCaMP6f cDNA was subcloned from SNAP25-GCaMP6f in the pEN_TmiR vector and recombined in the pSLIK-neo lentiviral vector [61]

using the Gateway System (Invitrogen). HeLa and HaCaT cells were then infected with the pSLIKneo-SNAP25-GCaMP6f vector and selected in a medium containing 400 µg/ml neomycin for seven days. CytoLuc-pGL3 basic (Promega #E1751), pLVX-NEO-CMV-2mt-GCaMP6s and SNAP25-Aequorin were kindly provided by Dr. Massimo Bonora and Dr. Paolo Pinton from the University of Ferrara [12, 62]. C1-MPAct-mCherry, CFP-CaaX and YFP-CaaX were gifts from Tobias Meyer (Addgene plasmids #155222, #155232, #155233;http://n2t.net/addgene:155222; RRID:Addgene_155222). For rescue experiments, we generated a cDNA of RTN3A resistant to RNAi oligo RTN3-2 by introducing 8 silent mutations by site-directed mutagenesis (oligo seq: GTTGATCATCCGCTTGTT) into the pBABE-HARTN3A construct. HeLa cells were infected with the pBABE-HA-RTN3A RNAi resistant form, and a clone expressing the transgene at endogenous levels was selected and used in reconstitution experiments. All clones were sequence-verified; details are available upon request.

Cell culture and transfection

HeLa (human cervix epithelial cells) cells were cultured in Minimum Essential Medium (MEM, Sigma) supplemented with 10% FBS, 2 mM glutamine, sodium pyruvate 1 mM (Euroclone), 0.1 mM non-essential amino acids (Euroclone). The pLVX-SNAP25-Luciferase HeLa clone was grown in the same medium as HeLa cells supplemented with 1 µg/ml Puromycin (Adipogen Life Sciences). The pSLIK-SNAP25-GCaMP6f and pLVX-mitoGCaMP6s HeLa clones were grown in the same medium as HeLa cells supplemented with 750 µg/ml G418 (Adipogen Life Sciences). HaCaT (human immortalized keratinocytes) and HeLa OSLO cells were cultured in DMEM medium (ThermoFisher) supplemented with 10% FBS and 2 mM glutamine. All cells were cultured at 37ºC and 5% CO_2. Cells were passaged every 2-3 days to maintain sub-confluency. HeLa cells at 50 – 60% confluence were transfected using FuGene (Promega) according to Manufacturer's instruction. Experiments were performed 24-48 h after transfection.

All human cell lines were authenticated at each batch freezing by STR profiling (StemElite ID System, Promega). All cell lines were tested for mycoplasma at each batch freezing by PCR (*32*) and biochemical assay (MycoAlert, Lonza).

RNA interference

RNAi was performed with Lipofectamine RNAimax (Invitrogen), according to the manufacturer's protocol: for RTN3 KD, RTN4 KD, NWASP KD and clathrin heavy chain KD, cells were transfected with 2 cycles (on day 1 in suspension, and on day 2 in adhesion) of 8 nM of oligos; for AP2µ1 KD, MCU KD and IP3-R1, IP3-R2, IP3-R3 KDs, 1 cycle of 8 nM of oligos; for Dynamin 1 and 2 KD, 1

cycle of 4 nM of oligo. Mock-treated cells (incubated with Lipofectamine RNAimax in optimum medium) were used as control. Experiments were performed 72 h after the second transfection. Oligo brand and sequence:

RTN3 Stealth Invitrogen	5'-CCCUGAAACUCAUUAUUCGUCUCUU-3'
RTN4 Stealth Invitrogen	5'-GGCGCCUCUUCUUAGUUGAUGAUUU-3'
Clathrin Heavy Chain Riboxx	5'-UAAAUUUCCGGGCAAAGAGCCCCC-3'
WASL ON-TARGET Plus Smart Pool Dharmacon	5'-CAGCAGAUCGGAACUGUAU-3' 5'-UAGAGAGGGUGCUCAGCUA-3' 5'-GGUGUUGCUUGUCUUGUUA-3' 5'-CCAGAAAUCACAACAAAUA-3'
IP3-R1 Smart Pool Riboxx	5'-UUAAACGAAAUGCUGCUCCCCC-3' 5'-AUAUGUAGAUGUUGUGCCCCC-3' 5'-AUAACUAGAUUGGAAGCCCCC-3'
IP3-R2 Smart Pool Riboxx	5'-UUAUUUCUUUCUGAGCAGCCCCC-3' 5'-AUUGAUACAAGAAACGGCCCCC-3' 5'-AUCUUUAACAUAACAGGCCCCC-3'
IP3-R3 Smart Pool Riboxx	5'-AUUAAGGUAAACUGAGUCCCCC-3' 5'-UUAUUCUUGUCAGUCCACGCCCCC-3' 5'-UAUAGAUGUUAUGGCCCACCCCC-3'
MCU Stealth Invitrogen	5'-GAUCAGGCAUUGUGGAAUAUAAGCU-3'
AP2µ1 Stealth Invitrogen	5'-CAUUGACCCGAAAGGCAUCCACUG-3'
Dynamin 1 Riboxx	5'-UUUCACAAUGGUCUCAAAGCCCCC-3'
Dynamin 2 Riboxx	5'-UGAACUGCAGGAUCAUGUCCCCC-3'

Western Blotting and Antibodies

Cells were lysed by adding RIPA buffer (50 mM Tris–HCl, 150 mM NaCl, 1 mM EDTA, 1% Triton X-100, 1% sodium deoxycholate, 0.1% SDS), plus protease inhibitor cocktail (CALBIOCHEM) and phosphatase inhibitors (20 mM sodium pyrophosphate pH 7.5, 50 mM NaF, 2 mM PMSF, 10 mM Na_3VO_4 pH 7.5) directly to cell plates and lysate was clarified by centrifugation at 13,200 rpm for 20 min at 4˚C. Protein concentration was measured by Bradford Assay (Biorad) and 20-50 µg of protein was run on 4-20% gradient pre-cast Gels (Biorad) and transferred using Trans-Blot (Biorad) according to manufacturer's instructions. Filters were blocked with 5% milk diluted in TBS 0.1% Tween20 (TBS-T) and then incubated overnight with primary antibody according to the datasheet. Following 3 washes with TBS-T, filters were then incubated with the appropriate secondary antibody conjugated with horseradish peroxidase. After 3 more washes, the signal was detected at Chemidoc (Biorad) using ECL from Amersham or Biorad.

Antibodies brands and dilutions:

Antibody	Producer	Clone or Epitope	Catalog Number	Usage	Dilution or concentration
EGFR 806	Homemade	aa 1172-1186 of human EGFR	REF[5]	WB	33 ng/ml
pY 1068 EGFR	Cell Signaling	Tyr 1068, D7A5	# 3777 (XP)	WB	1:1000
pY 992 EGFR	Cell Signaling	Tyr 992	#2235	WB	1:1000
SHC	BD	Clone 20	#610878	WB	1:500
pSHC	Cell Signaling	Tyr239/240	#2434	WB	1:500
AKT	Cell Signaling		#9272	WB	1:1000
pAKT	Cell Signaling	Thr308	#9275	WB	1:500
ERK1/2	Sigma	ERK-1, 351-368	M7927	WB	1:5000
pERK1/2	Cell Signaling	Thr202/Tyr204	#9106	WB	1:1000
Vinculin	Sigma	clone hVIN-1	V9131	WB	1:5000
GAPDH	Santa Cruz	6C5	sc-32233	WB	1:3000
gamma-Tubulin	Homemade	Serum		WB	1:1000
EGFR	Genentec	Clone 13A9	13A9	IF/EM	1:2000
HGFR	R&D	Glu25-Thr932	AF276	IF	1:200
CD147	BD	HIM 6	555961	In vivo IF	1:300
TOMM20	Novus Biologicals		NBP1-81556	CLEM	1:100
Clathrin Heavy Chain	BD	Clone 23	610499	WB	1:1000
MCU	Sigma		HPA016480	WB	1:500
IP3-R1	Millipore		AB5882	WB	1:1000
IP3-R2	Novus		NB100-2466	WB	1:500
IP3-R3	BD		610312	WB	1:4000
RTN3	Homemade	aa 1-47, common to all RTN3 isoforms		WB	1.5 µg/ml
RTN4	Novus		NB100-5668155	WB	1:500
AP2 p50µ	Transduction BD		m2	WB	1:100
N-WASP	Santa Cruz	H100	sc20770	WB	1:100
FITC-Tyramide	Akoya Biosciences		SKU SAT701001EA	CLEM	1:100

Firefly Luciferase	Invitrogen		PA5-32209	IF WB	1:250 1:500

CD147/EGF/Tf – HGFR/HGF internalization assays

For antibody internalization assays, serum-starved cells were first incubated with anti-CD147 antibody for 60 min at 4˚C and then with an Alexa-488 fluorescent secondary antibody (in green) for 30 min at 4˚C. Cells were then stimulated with high dose Alexa-conjugated EGF (see section "EGF concentration") at 37˚C for 5 min in HeLa cells and 12-15 min for HaCaT cells, or with high dose unlabeled HGF (1 µg/ml, preactivated for 20 min at room temperature followed by 15 mins at 37°C in 100% serum, then diluted in serum-starved medium for obtaining a final concentration of 100 ng/ml in 10% serum prior to use) for 8 min. As a control, we also incubated CD147 in the absence of the ligand (in the case of HGF experiment, in the presence of 10% serum) and we observed no detectable CD147 internalization. After internalization, cells were acid wash-treated (100 mM Glycine-HCl) pH 2.2, fixed in 4% paraformaldehyde and processed for IF. Images were obtained using a Leica TCS SP8 confocal microscope equipped with a 63X oil objective and processed using ImageJ. An *ad hoc* designed macro was used to quantify CD147 signal upon stimulation with EGF[5]. CD147 signal was highlighted applying an intensity-based threshold (Default method), and then fluorescence intensity per field was calculated using the "Measure" command, limiting measurements to threshold. This value was then divided by the number of nuclei in the field, counted using the DAPI signal, to calculate the CD147 fluorescence intensity per cell.

For HGFR internalization assay, HeLa cells were stimulated with high dose HGF at 37 °C for 8 min as described above. Following fixation, HGFR protein was stained with anti-HGFR antibody recognizing the extracellular domain followed by CY3-labelled secondary antibody before permeabilization (referred to as PM HGFR). After staining, the cells were further fixed and then permeabilized to allow for another round of staining with anti-HGFR antibody followed by Alexa 647-labelled secondary antiboby (referred to as Total HGFR). The resulting images were analyzed using ImageJ software. The PM HGFR signal was selectively emphasized by applying an intensity-based threshold using the "Otsi" method. The fluorescence intensity per field was then calculated using the "Measure" command, with measurements limited to the thresholded region. A similar analysis was performed for the Total HGFR signal using the "Moments" method. Finally, the ratio of PM HGFR to Total HGFR was used to normalize the levels of PM HGFR in each experimental condition.

To quantify internalized EGF/Tf, cells were stimulated with high dose Alexa-conjugated EGF or Alexa-conjugated Tf (see section "EGF concentration") at 37 °C for 5 min (EGF) or 8 min (TF) in

HeLa cells, and 12 min for both ligands in HaCaT cells. Before fixation, samples were subjected to acid wash treatment to visualize only internalized ligand. Images were analyzed using ImageJ. EGF signal was highlighted applying a 10-intensity based threshold (Default method), and then fluorescence intensity per field was calculated using the "Measure" command, limiting measurement to threshold. This value was then divided for the number of nuclei in the field, counted using the DAPI signal to calculate the EGF fluorescence intensity per cell.

Electron microscopy

Pre-embedding immunolabeling. Serum-starved cells were incubated with anti-EGFR 13A9 (Genetech) or with anti-CD147 antibody, followed by incubation with rabbit anti-mouse, and, finally, with Protein-A Gold 10 nm (30 min incubation on ice/each step). Cells were then incubated at 37°C for 5 min with 30 ng/ml EGF, as indicated. A control sample left at 37°C for 5 without EGF was included in the experiment to control that no internalization was induced by the antibody in the absence of ligand. Cells were then washed in PBS and fixed for 1 h at room temperature in 1.2% glutaraldehyde in 66 mM sodium cacodylate buffer pH 7.2 containing 0.5 mg/ml of ruthenium red. After quick washes with 150 mM sodium cacodylate buffer, the samples were post-fixed in 1.3% osmium tetroxide in a 66 mM sodium cacodylate buffer (pH 7.2) containing 0.5 mg/ml ruthenium red for 2 h at room temperature. Cells were then rinsed with 150 mM sodium cacodylate, washed with distilled water and enbloc stained with 0.5% uranyl acetate in dH_20 overnight at 4°C in the dark. Finally, samples were rinsed in dH_2O, dehydrated with increasing concentrations of ethanol, embedded in Epon and cured in an oven at 60°C for 48 h.

Ultrathin sections (70 – 90 nm) were obtained using an ultramicrotome (UC7, Leica microsystem, Vienna, Austria), collected, stained with uranyl acetate and Sato's lead solutions, and observed in a Transmission Electron Microscope Talos L120C (FEI, Thermo Fisher Scientific) operating at 120 kV. Images were acquired with a Ceta CCD camera (FEI, Thermo Fisher Scientific). *Morphometry of NCE TIs and of CCPs.* Cellular profiles of thin sections of cells immunolabeled with anti-EGFR or with anti-CD147 antibodies and stained with ruthenium red were acquired. Endocytic structures were classified as NCE TIs or CCPs depending on their morphology and the presence of a clathrin coat. The distance of gold-positive/ruthenium red-positive endocytic structures to the PM was measured with ImageJ and the ratio between short and elongated structures for each cellular profile was calculated (NCE TIs: short 150-300 nm; elongated > 300 nm; CCPs: short <200 nm elongated > 200 nm).

KDEL-HRP/DAB visualization of ER. Cells were fixed in 1% glutaraldehyde in 0.1 M sodium cacodylate buffer (pH 7.4) for 30 min at room temperature, followed by incubation with 0.3 mg/ml 3,3'-diaminobenzidine tetrahydrochloride (DAB) and 0.03% hydrogen peroxide in 0.1 M sodium cacodylate buffer pH 7.4 for 20 min at room temperature. Samples were rinsed in sodium cacodylate buffer and post-fixed with 1.5% potassium ferrocyanide, 1% osmium tetroxide in 0.1M sodium cacodylate buffer (pH 7.4) for 1 h on ice. After enbloc staining with 0.5% uranyl acetate in dH_20 overnight at 4°C in the dark, samples were dehydrated with increasing concentrations of ethanol, embedded in Epon and cured in an oven at 60°C for 48 h. Ultrathin sections (70 – 90 nm) were obtained using an ultramicrotome (UC7, Leica microsystem, Vienna, Austria), collected, stained with uranyl acetate and Sato's lead solutions, and observed in a Transmission Electron Microscope Talos L120C (FEI, Thermo Fisher Scientific) operating at 120 kV. Images were acquired with a Ceta CCD camera ((FEI, Thermo Fisher Scientific).

Serial Section Electron Tomography. Serial thick sections (130-150 nm) were collected on formvar-coated copper slot grids. Gold fiducials (10 nm) were applied on both surfaces and the grids were stained with 2% methanolic uranyl acetate and Sato's lead citrate. The samples were imaged using a 120 kV Talos L120C (Thermo Fisher Scientific). Tilted images (+65/−65 according to a Saxton scheme) were acquired with Tomography 4.0 acquisition software (Thermo Fisher Scientific) using a 4kx4k Ceta16M camera (Thermo Fisher Scientific). Tilted series alignment, tomography reconstruction, and serial tomograms joining were performed using the IMOD software package (Mastronarde, 1997).

3D ER-mitochondria visualization and quantification. Tomograms were semi-automatic segmented using Microscope Image Browser (MIB) (DOI: 10.1371/journal.pbio.1002340). ER stained by KDEL-HRP/DAB electron dense precipitate was segmented using MIB Frangi Filter; mitochondria and PM were manually segmented with the brush tool on few slices and automatically interpolated through the 3D stacks. For visualization, the MIB model was exported to IMOD. For quantification, the segment profiles were exported to MatLab (MathWorks Inc.) and the distances between ER and mitochondria profiles were calculated with a MatLab script.

ER-Mitochondria contact site analysis. HRP-KDEL[5, 63] transfected cells were fixed with 4% paraformaldehyde, 0.01% Glutaraldehyde in 0.1M Hepes pH 7.4. The ER was then visualized incubating the cells using fluorescent tyramide (TSA-FITC 1:200, AKOYA Biosciences), 0.003 H_20_2 and 0,05% Tween-20 in 100 mM borate buffer. Cells were then permeabilized with 0.1% saponin and

stained with TOMM20 antibody (NBP1-81556 from Novus Biologicals) visualized with a secondary antibody conjugated with Alexa564 (Invitrogen). Samples were then dehydrated and embedded in LR white resin using microwave irradiation. Ultrathin sections (100 nm) were obtained with a Leica UC7 ultramicrotome, collected on glass coverslips and nuclei were stained with Hoechst. The fluorescence signal was collected in a DeltaVison widefield microscope (DeltaVision Elite; Applied Precision/GE Healthcare) using a 100x plan-apo oil immersion objective. The acquired 3D stack was deconvoluted using software (DeltaVision Elite; Applied Precision/GE Healthcare) and analyzed with ImageJ software. ER-mitochondria "contacts" were identified with the object-based colocalization function of JaCop Plugin[64]. To quantify juxtamembrane contacts using the Hoechst channel, nuclei and the cell borders were manually segmented and a relative distance map was created having a value of 0 close to the nucleus and 1 close to the cell border. Contacts in proximity to the PM (relative distance map value higher than 0.75) were identified using ImageJ Analyze particles plugin.

To validate the quantification procedure used the CLEM approach evaluating whether the colocalization regions identified with ImageJ corresponded to a real contact site at EM level. To make the fluorescent section compatible with EM imaging we introduced in the embedding procedure heavy metal staining. Briefly, after KDEL-HRP/TSA staining and TOMM20 immunolabeling, cells were post-fixed with 0.2% osmium tetroxide, 0.3% potassium ferrocyanide in 0.1 M cacodylate buffer for 5 min with microwave irradiation (two microwave pulses of 40 sec over 5 min). Then samples were further contrasted with 0.5% uranyl acetate for 1 min in the microwave and finally dehydrated and embedded in LR white resin. This procedure confers to the sample enough contrast enabling the visualization of the cellular membrane during EM imaging but decreased the fluorescent signal. Therefore, for the CLEM approach, we used mitotracker staining for mitochondria visualization since it gave a brighter signal compared to TOMM20 immunostaining. Ultrathin sections (100 nm) were obtained with a Leica UC7 ultramicrotome, collected on glass coverslips, and nuclei were stained with Hoechst and imaged with a DeltaVision widefield microscope. After being imaged, the sections were detached from the glass coverslips using 1% hydrofluoric acid and collected on formvar-carbon coated slot grids. The same cell acquired in the fluorescence microscope was then identified at the EM level and images were collected with a Talos L120C transmission electron microscope. Fluorescent and EM images were aligned with ec-clem ICY plugin, and the number of contact sites revealed by EM (20 nm distance) and fluorescence (JaCoP plugin) were evaluated.

Measurements of intracellular Ca^{2+} concentration

Aequorin measurements. HeLa cells grown on 13-mm-round glass coverslips at 50% confluence were transfected with the appropriate PM-targeted aequorin chimeras. Aequorin constructs and protocols were previously described[19]. All aequorin measurements were performed in KRB buffer (135 mM NaCl, 5 mM KCl, 0.4 mM KH_2PO_4, 1 mM $MgSO_4$, 20 mM HEPES and 5.5 mM glucose, pH 7.4), supplemented with 1 mM Ca^{2+}. When EGTA treatment was performed, aequorin measurements were recorded in KRB buffer plus 100 µM EGTA. Stimulation with EGF was performed as specified in the Figure legends. The experiments were terminated by lysing the cells with 0.01% Triton in a hypotonic Ca^{2+}-rich solution (10 mM $CaCl_2$ in H_2O), thus discharging the remaining aequorin pool. The light signal was collected and calibrated into $[Ca^{2+}]$ values, as previously described[19]. Extent of Ca^{2+} waves was expressed as area under the curve (AUC) and maximal value of peak in box plot graphs (whiskers min to max). Statistical analysis was performed using GraphPad Prism.

GCaMP measurements were performed using two different fluorescent Ca^{2+}-probe with different affinity for Ca^{2+}: GCaMP6f and GCaMP6m[12, 36, 62]. GCaMPs were developed for imaging rapid Ca^{2+} peaks, like the one observed at ER-PM NCE contact sites. To localize the probe to the PM, where NCE contact sites are formed, we added the PM-targeting sequence of SNAP25, as used for Aequorin [5]. GCaMP-stable HeLa clones (PM-GCaMP6f and mitoGCaMP6m) were grown on 35-mm coverslips or MatTek 48 h prior to the acquisition of images. PM-GCaMP6f cells were subjected to 0.5 µg/ml overnight doxycycline induction the day before the recording of the experiment. For image acquisition, cells were washed and kept in KRB buffer supplemented with 1 mM Ca^{2+} and glucose. To determine the PM Ca^{2+} response, cells were placed on a 37˚C thermostat-controlled stage and exposed to 490/406 nm wavelength light using the Olympus fluorescent microscopy system equipped with a 20x oil objective acquiring 5fps for a total of 6 min. After recording baseline ratio, cells were stimulated with EGF under the indicated conditions. To assess the PM Ca^{2+} response after HGF stimulation, HeLa cells were rinsed once with KRB buffer and allowed to adapt for approximately 5 min in KRB buffer supplemented with 1% serum to activate HGF. Similarly, for EGF experiments, the cells were placed on a 37˚C thermostat-controlled stage and exposed to light of 490/406 nm wavelength. After measuring the baseline ratio, the cells were stimulated with 250 ng/ml HGF, which was diluted in PBS-0.1%BSA. This same PBS-0.1%BSA solution was used as the control in the absence of HGF (-HGF condition). Fluorescent data collected were expressed as emission ratios. The increase in intensity was calculated with ImageJ using an *ad hoc* designed macro and the extent of Ca^{2+} peaks was expressed as AUC and maximal value of peak in box plot graphs (whiskers min to max). Statistical analysis was performed using GraphPad Prism.

Measurements of mitochondrial membrane potential with TMRM dye

Cells were grown on 35-mm round glass MatTek at 50% confluence the day before the experiment and then incubated with 1 nM TMRM dye (Catalog Number I34361, T668 Invitrogen) diluted in DMEM without FBS and red phenol supplemented with 2 mM L-glutamine and 25 µM verapamil (V4629, CAS 152-11-4, Sigma Aldrich) for 1 h at 37˚C and 5% CO_2. Then, the variation in the intensity of the dye was monitored by time-lapse microscopy. A Leica TCS SP8 AOBS inverted microscope with 20× oil objective was used to take pictures every 2 sec over a 5 min period. The assay was performed using an environmental microscope incubator set to 37°C and 5% CO_2 perfusion. After cell incubation with the dye, EGF at the indicated doses was added and maintained in the media for the total duration of the time-lapse experiment. To evaluate changes in TMRM levels following HGF stimulation, cells were incubated with a 10 nM diluted solution of the dye in DMEM without red phenol, supplemented with 1% serum, 2 mM L-glutamine, and 25 µM verapamil. HGF, pre-activated in the same solution used for cell incubation, was then introduced to reach a final concentration of 100 ng/ml and remained in the media throughout the entire time-lapse experiment. The same DMEM without red phenol supplemented with 1% serum, 2 mM L-glutamine, and 25 µM verapamil solution was used as the mock control in the absence of HGF (-HGF condition). The increase in intensity was calculated with ImageJ using an *ad hoc* designed macro and the extent of the difference in mitochondrial potential was expressed as AUC and maximal value of peak in box plot graphs (whiskers min to max). Statistical analysis was performed using GraphPad Prism.

Measurements of PM-localized ATP production with SNAP25-Luciferase (PM-Luc)

The pLVX-SNAP25-Luciferase HeLa cells were grown on 13-mm-round glass coverslips at 50% confluence and then analyzed by an IVIS luminometer. The system is composed of an upper part containing a highly sensitive photomultiplier arranged in a metal dark box to protect it and the temperature-controlled chamber from light exposure. The chamber (2 mm height and 265 µl volume) houses the cell sample seeded on a 13 mm-diameter coverslip during ATP measurement which was placed close to the photomultiplier. Cells were continuously perfused with temperature-controlled solutions in a water bath at 37°C. A peristaltic pump allowed for liquid perfusion [65]. The three-phase acquisition started with 30 sec of background recording in DMEM without red phenol (Lonza) supplemented with 2 mM L-glutamine. Then, the cell population was perfused with 25 µM beetle D-luciferin (Promega, E1601). Within 2–3 min, luciferase catalyzes light production, reaching a plateau after reacting with intracellular ATP. In the end, cells were perfused with EGF at the desired concentration and recorded for 2-3 min. The output signal was recorded and converted to kinetics via

Hamamatsu Photonics software and the extent of the ATP was expressed as AUC in box plot graphs. Statistical analysis was performed using GraphPad Prism.

CD147 internalization rescue experiment with histamine and succinate

Cells were subjected to MCU KD or mock transfection (see section "RNA interference"). After 4 days, control and MCU KD cells were seeded on 13-mm-round coverslips at 40-50% of confluency and CD147 internalization assay was performed (see section "CD147 internalization assay"). After the release of CD147 from 4˚C to 37˚C, cells were incubated with 10 µM histamine (Sigma) or pre-treated for 5 min and then incubated with 5 mM succinate (Sigma), or both in combination, either with or without high dose EGF. After internalization, cells were acid wash-treated and then fixed and processed for IF. Images were obtained using a Leica TCS SP8 confocal microscope equipped with a 63× oil objective and processed using ImageJ using an *ad hoc* designed macro (see section "CD147 internalization assay")[5].

Cortical Actin polymerization with MPAct/CaaX

Cells were seeded in 10 mm plates at 60% of confluence in complete medium and then co-transfected with MPAct mCherry and YFP-CaaX vectors (selected plasmid constructs, corresponding sequence information is available on Addgene) [35]. After 36 h, transfected cells were seeded on 13 mm-round coverslips at a confluence of 40-50%. Cells were then stimulated with the indicated doses of EGF at 37˚C for 5 min. As a control, we also kept cells at 37˚C in the absence of the ligand, to set the basal levels of F-actin polymerization proximal to the PM. After internalization, cells were fixed and processed for IF. Images were obtained using a Leica TCS SP5 or TCS SP8 confocal microscope equipped with a 63× oil objective and processed using ImageJ. The membrane proximal actin (MPAct) value was generated by subtracting the background to each channel and then calculating the ratio of the MPAct/CaaX channels using an *ad hoc* designed macro. Ratiometric MPAct over CaaX intensities (here termed MPAct/CaaX) was used to measure relative local spatial heterogeneities in MPA density along the cell surface. Statistical analysis was performed using GraphPad Prism.

Wound healing assay

HaCaT cells were seeded in 24-well plates equipped with proprietary treated plastic inserts (2.5×10^5 cells per well) in complete medium and cultured until a uniform monolayer was formed. The inserts create a wound field with a defined gap of 0.9 mm for measuring the migratory rates of cells. The cell monolayer was scratched by carefully removing the plastic inserts and washed twice with 1X PBS to remove floating cells and to create a cell-free wound area. The closure of the wound was

monitored by time-lapse video microscopy. A Nikon Eclipse Ti inverted microscope with 10× N2 objective was used to take pictures every 5 min over a 24 h period (as indicated in the figure legends). The assay was performed using an environmental microscope incubator set to 37 °C and constant 5% CO_2 perfusion. After the scratch, EGF at the indicated doses was maintained in the serum-starved media for the total duration of the time-lapse experiment. The wound front speed was calculated using Image J software. For the assay performed on interfered cells, cells were interfered following the same conditions already described in the 'RNA interference' section, plated the day before the experiment and stimulated in serum-starved medium supplemented with EGF at the indicated concentration.

TPEF microscopy

For TPEF microscopy, cells were cultured on 22x22x0.17 mm quartz slides (UQG Optics, United Kingdom). Three biological replicates were produced per each condition (-EGF, Control/High EGF, and RTN3 KD/High EGF. Cells were fixed in paraformaldehyde 4% and stored at 4 °C. Prior to measurements, each quartz slide was mounted upside-down and sealed with a second 25x50x0.17 mm quartz slide (UQG Optics, United Kingdom), with cells placed in-between the two slides. We employed a home-built multimodal optical microscope featuring epi-detected Two-Photon Excited Fluorescence (TPEF), along with linear transmission light. This setup has been described in detail elsewhere[23, 66]. Briefly, a compact Erbium-fiber multi-branch laser source (FemtoFiber Pro, Toptica Photonics, Germany) delivers 1560 nm pulses at a 40 MHz repetition rate with < 100 fs duration. One branch is frequency-doubled to deliver narrowband 780-nm pump pulses, whereas a second branch (Stokes beam) is spectrally broadened and then frequency-doubled to allow the generation of tunable picosecond pulses in the 950-1050 nm range. Both the resulting beams feature a ≈ 1-picosecond duration. The average laser power at the sample plane is kept constant at 7.5 mW for the pump, and 0.5 mW for the Stokes, throughout the study, which limits cell photodamage ensuring non-invasiveness. The pump beam is used to excite TPEF interactions, whereas the red-shifted low-power Stokes beam at 1003 nm is used to obtain transmission images of the samples. The inverted-configuration microscopy unit includes high numerical aperture (NA) objectives that ensure subcellular spatial resolution (~280 nm lateral resolution, ~300 nm axial resolution, as for the Rayleigh criterion applied to nonlinear optical imaging): a water-immersion 100X 1.25NA 0.25 mm working distance (WD) illumination objective (C-Apochromat, Carl Zeiss, Germany) and an oil-immersion 40X 1.35NA 0.19 mm WD (CFI Super Fluor, Nikon, Japan) collection objective. The x-y-z motorized sample stage (Standa, Lithuania, and Mad City Labs Inc, U.S.A.) can scan large areas (up to 50x50 mm^2) while keeping the sample in focus. A photo-multiplier tube (PMT) (Hamamatsu

Photonics, Japan) detects TPEF in the range 400-600 nm through optical filtering (FES0600, ThorLabs, Germany) at its inlet. The transmitted Stokes intensity is detected through a photodiode to obtain transmission images. All cell images in the present study have a dimension of 70x70 μm^2, 200x200 pixels (i.e., a pixel size of 350x350 nm). A 1.5-ms pixel dwell time is employed for image acquisition.

TPEF image analysis

Images were processed via the Fiji-ImageJ software for image analysis. Both dark and bright 1-pixel outliers were median-filtered in order to correct extreme pixel values given by cosmic rays. An automated circular shift of image columns is used to compensate for distortion effects due to the serpentine-like motion of the motorized sample stage. The linear transmission of the Stokes is used to differentiate cells from the substrate and outline the cell area since cells appear as relatively dark regions due to a drop in laser transmission. As for mitochondrial NAD(P)H and FAD distribution, it was quantified from raw TPEF images acquired with constant integration time and laser power. A universal threshold of 0.75 a.u. was set to distinguish the endogenous signal from the diffused background that is presented outside of cells. The calculated percentage index of TPEF distribution inside cells is obtained as the ratio of TPEF area [μm^2] after signal thresholding over cell area [μm^2]. TPEF images are here displayed collectively normalized (TPEF signal range: 0-1).

Statistical analysis

All statistical analyses were performed using GraphPad Prism. Two-sided student's T-test was employed to obtain statistical significance of experimental differences. Non-parametric U-Mann Whitney test was used to evaluate the statistical significance of TPEF distribution in cell populations. For both tests, p-value <0.05 *, p-value <0.01 **, p-value <0.005 ***, p-value <0.001 ***.